Monthly Notices
of the
ROYAL ASTRONOMICAL SOCIETY

MNRAS **472,** 419–438 (2017)
Advance Access publication 2017 June 26

doi:10.1093/mnras/stx1579

Chronos and KAIROS: MOSFIRE observations of post-starburst galaxies in $z \sim 1$ clusters and groups

B. C. Lemaux,[1⋆] A. R. Tomczak,[1] L. M. Lubin,[1] P-F. Wu,[2] R. R. Gal,[3] N. Rumbaugh,[1,4] D. D. Kocevski[5] and G. K. Squires[6]

[1]*Department of Physics, University of California, Davis, One Shields Ave., Davis, CA 95616, USA*
[2]*Max-Planck Institut für Astronomie, Königstuhl 17, D-69117, Heidelberg, Germany*
[3]*University of Hawai'i, Institute for Astronomy, 2680 Woodlawn Drive, Honolulu, HI 96822, USA*
[4]*Department of Physics and Astronomy, Colby College, Waterville, ME 04961, USA*
[5]*Spitzer Science Center, California Institute of Technology, M/S 220-6, 1200 E. California Blvd., Pasadena, CA 91125, USA*
[6]*National Center for Supercomputing Applications, University of Illinois, 1205 West Clark St., Urbana, IL 61801, USA*

Accepted 2017 June 21. Received 2017 June 21; in original form 2016 July 29

ABSTRACT

We present an exploration of ∼500 spectroscopically confirmed galaxies in and around two large-scale structures (LSSs) at $z \sim 1$ drawn from the Observations of Redshift Evolution in Large Scale Environments survey, an ongoing, wide-field photometric and spectroscopic campaign targeting a large ensemble of LSSs at $0.6 < z < 1.3$. A sub-sample of these galaxies (∼150) was targeted for the initial phase of a near-infrared MOSFIRE spectroscopic campaign investigating the differences in selections of galaxies that had recently ended a burst of star formation and/or had rapidly quenched (i.e. post-starburst/K+A galaxies). Selection with MOSFIRE utilizing the Hα and [N II] emission features resulted in a post-starburst sample more than double that selected by traditional $z \sim 1$ (observed-frame optical) methods even after the removal of the relatively large fraction of dusty starburst galaxies selected through traditional methods. While the traditional post-starburst fraction increased with increasing global density, the MOSFIRE-selected post-starburst fraction was found to be constant across field, group, and cluster environments. However, this fraction computed relative to the number of star-forming galaxies was observed to elevate in the cluster environment. Post-starbursts selected with MOSFIRE exhibited moderately strong [O II] emission originating from activity other than star formation. Such galaxies, termed K+A with ImposteR [O II]-derived Star formation (KAIROS) galaxies, were found to be younger than and likely undergoing feedback absent or diminished in their optically selected counterparts. A comparison between the environments of the two types of post-starbursts suggested a picture in which the evolution of a post-starburst galaxy is considerably different in cluster environments than in the more rarefied environments of a group or the field.

Key words: galaxies: evolution – techniques: photometric – techniques: spectroscopic – galaxies: clusters: general – galaxies: groups: general – galaxies: starburst.

1 INTRODUCTION

It has been evident since both the earliest observations of nearby clusters of galaxies and the initial modelling of these clusters that the environment in which a galaxy resides dictates, to some extent, its fate (Gunn & Gott 1972; Oemler 1974; Butcher & Oemler 1978; Dressler 1980). Studies of enormous samples of field, group, and cluster galaxies residing in the local universe made possible by the Sloan Digital Sky Survey (SDSS; York et al. 2000) have reaffirmed these early observations; galaxy populations that reside in higher density environments almost universally have a larger fraction of red, quiescent early-type galaxies than those populations inhabiting more rarefied environments (e.g. Gómez et al. 2003; Goto et al. 2003a,b; Hansen et al. 2009). While this correlation appears, generally, to hold up to $z \sim 1$ (Papovich et al. 2010; Strazzullo et al. 2010; Cooke et al. 2016) at least for the most massive overdensities, strong differential evolution is observed in the quiescent fraction between overdense and more typical regions of the universe (e.g. Cooper et al. 2007; Cucciati et al. 2017). At earlier epochs, with some exceptions, the fraction of redder or passive galaxies

⋆E-mail: bclemaux@ucdavis.edu

appears to decrease appreciably in overdense environments reaching levels indistinguishable from or beneath that of the field population (e.g. Lin et al. 2016; Wang et al. 2016). Correspondingly, an increase in the average star formation rate (SFR) of galaxies residing in overdense environments is observed, with the relationship between SFR and density flattening (e.g. Zeimann et al. 2013; Ziparo et al. 2014) or, in some cases, reversing (e.g. Tran et al. 2010; Santos et al. 2014, 2015; Dey et al. 2016) at $z \gtrsim 1$ relative to the anti-correlated behaviour observed in the local universe. In tandem, strong differential evolution between the field and overdense environments is observed in the fraction of galaxies undergoing strong transient activity, such as those hosting a particularly prodigious star-formation event (Kocevski et al. 2011; Webb et al. 2013) or a powerful active galactic nuclei (AGNs; Martini et al. 2013; Alberts et al. 2016). Given the large number of processes that serve to either induce or quench star formation activity in group and cluster environments, which are either not present or considerably less effective in more typical environments, it is easy to adopt the naive view that environment is *the* fundamental quantity in governing the evolution of a galaxy both at early and late times in the history of the universe.

However, this simplistic view is challenged in a variety of respects. Large spectroscopic and photometric samples of galaxies from $0 < z < 4$ predominantly located in field environments have unequivocally shown that separate processes that appear largely independent of or only circumstantially connected with environment can act effectively to transform blue, star-forming, late-type galaxies to red, quiescent, early types (Bundy et al. 2006; Faber et al. 2007; Pozzetti et al. 2010; Ilbert et al. 2010, 2013; Davidzon et al. 2013). Such processes appear to be intimately connected, whether circumstantially or causally, to the stellar mass content of galaxies. It is observed in both the local (Peng et al. 2010; Deng et al. 2011) and the higher-redshift universe (Muzzin et al. 2012; Darvish et al. 2016) that the average SFR per unit stellar mass (specific star formation rate, SSFR) of star-forming galaxies is constant at fixed stellar mass as a function of environment (though this trend may depend on the method used to estimate environment; see Noble et al. 2016). Conversely, the average SSFR is found to be a strong function of stellar mass in both the local and distant universe. In a study of several thousands of galaxies from $z = 0 - 1$, Peng et al. (2010) inferred based on a simple empirical model that (stellar) massive galaxies ($\log(\mathcal{M}_*/M_\odot) > 10.2$) are much more likely to be quenched via stellar-mass-related processes than those related to environment. Lending credence to this picture is the observed similarity in the stellar mass function of *both* quiescent and star-forming galaxies in the field relative to those galaxies residing in more dense environments (e.g. van der Burg et al. 2013; Vulcani et al. 2013). These observations seem to require that, if environmentally driven quenching is to occur, it must, once begun, operate over a relatively rapid time-scale in order to preserve these trends. Such a scenario is supported by several recent studies that have, through a variety of different methods, attempted to constrain the star formation histories (SFHs) of local and $z \sim 1$ group and cluster galaxies (Wetzel et al. 2013; Mok et al. 2014; Muzzin et al. 2014; Balogh et al. 2016) finding that, after a relatively long delay, truncation of star formation must be rapid (∼0.1–0.8 Gyr) to simultaneously fit data, models, and simulations (though see e.g. Taranu et al. 2014 for an alternative view). Conversely, such a feature is not required in the SFHs of field galaxies. Thus, it appears that the most promising avenue of inquiry to observe and constrain environmentally driven quenching is in galaxies that have undergone recent, dramatic changes in their star formation properties.

While several candidate populations exist, e.g. red spirals (Moran et al. 2007; Bundy et al. 2010; Masters et al. 2010), galaxies selected with colours intermediate to star-forming and quiescent populations (Balogh et al. 2011; Schawinski et al. 2014), rejuvenated lenticular or spheroid galaxies (Treu et al. 2005; Kannappan, Guie & Baker 2009), one population, in particular, has been given particular attention over the past several decades. Early studies of intermediate redshift clusters revealed a modestly large population of galaxies with spectral features indicative of a lack of ongoing star formation and a large number of recently formed stars added to an older underlying stellar population (Dressler & Gunn 1983; Couch & Sharples 1987; Dressler & Gunn 1992). Such a spectrum is only possible for a galaxy that has recently undergone a star-formation event vastly exceeding its past-averaged star formation activity (hereafter 'starburst') or rapid quenching (or both), necessarily meaning such galaxies have necessarily undergone a violent transformation in the recent past. These galaxies, eventually termed 'K+As after the two primary stellar types observed in their spectra,[1] became the subject of intensive searches across all environments in both the local and distant universe. Initial searches found a considerable fractional excess of K+A galaxies inhabiting massive clusters at moderate redshift relative to the coeval field (e.g. Belloni et al. 1995; Dressler et al. 1999; Tran et al. 2003), which led to speculation that cluster-related processes were essential to induce the strength of burst or the rapidity of the quenching needed to induce a K+A phase. Later studies showed that inhabiting a cluster environment was not necessarily a requisite condition, as K+As were also found in more rarefied environments such as groups and, in some cases, the field (Zabludoff et al. 1996). While some more recent studies have found that K+A galaxies are, by fraction, more likely to inhabit the cluster environment at $z \sim 1$ (Poggianti et al. 2009; Muzzin et al. 2012; Wu et al. 2014), several studies have found a relatively large fraction of K+As in the field at these redshifts (Wild et al. 2009; Yan et al. 2009; Vergani et al. 2010), again precluding the possibility that cluster-specific processes are solely responsible for generating this evolutionary phase.

Howevever, the extreme rarity of the K+A population and the lack of campaigns targeting overdense environments at $z \sim 1$ with coverage analogous to wide-scale coeval field surveys at $z \sim 1$ (e.g. Lilly et al. 2007; Le Fèvre et al. 2013; Newman et al. 2013) make such trends highly subject to sample variance as well as the depth and breadth of the spectroscopic coverage. Perhaps the most pernicious difficulties in interpreting these trends comes in the form of the choice of metrics used to define environment (local versus global), various controls or lack thereof on the sample (volume-limited versus flux-limited, luminosity-limited versus stellar mass limited), and the method by which K+A galaxies are selected. Approached carefully, the former two issues are perhaps easier to mitigate. While quenching mechanisms appear to have a complex relationship with local density, halo mass, dynamical state of the parent halo, stellar mass, and various photometric and spectroscopic limits, such limitations can be broadly controlled for with relative ease by making completeness corrections to the sample, incorporating appropriate sample variance uncertainties, or by making proper internal comparisons. The issue of differing K+A selection, however, is not correctable by these approaches as differing selections of

[1] Though these galaxies are sometimes termed 'post-starburst, it should be clear from the definition that a starburst is not required to generate the K+A phase. Regardless, we irresponsibly use the two terms interchangeably throughout the paper.

galaxies classed 'K+A' can fundamentally change the galaxy population being probed and, by consequence, the conditions that the selected population is experiencing. While promising progress has been made on selecting K+A populations photometrically (Wild et al. 2014; Maltby et al. 2016), such methods are still maturing, and, thus, we limit our discussion here to K+As selected spectroscopically. There are several issues with the canonical selection of K+A galaxies at higher redshift ($z \sim 1$), and they are primarily related to the requirement that K+A galaxies have no ongoing star formation. While exceptions exist, the vast majority of $z \sim 1$ studies of K+A galaxies require the absence of the [O II] λ3727 Å line in order to classify a galaxy as K+A. Such a requirement carries with it a variety of issues related to purity and completeness. The criterion or criteria used to set the limit for the non-detection of [O II] line is highly dependent on the signal to noise (S/N) and resolution of the observed spectra. A minimal change at fixed S/N and resolution can lead to the selection of dramatically different populations (e.g. Wu et al. 2014). Equally importantly, the [O II] line is highly subject to differential extinction and can be emitted, copiously so, by processes other than star formation leaving open the possibility that even those $z \sim 1$ K+A samples selected using an [O II] cut appropriate for their data will be composed of a large number of dusty starburst galaxies (false positives) and will exclude a large number of galaxies with post-starburst features that are emitting [O II] for a reason other than star formation (false negatives).

In this study we investigate a large population (∼500) of galaxies in and around two large-scale structures (LSSs) at $z \sim 0.8$ targeted with observed-frame optical spectroscopy, of which ∼150 were followed up with near-infrared (NIR) spectroscopy. These samples are additionally complemented by deep 10+ band optical/NIR and X-ray imaging. With these observations, we investigate the effects of completeness and purity in traditionally selected K+A populations in both the field and overdense environments and the consequences for the inferences on quenching mechanisms in such environments. The paper is organized as follows. Section 2 discusses the structures targeted in this study and lists the properties of our optical/NIR imaging and spectroscopy. In Section 3, we discuss the various analyses used to approach the analysis of K+A and other galaxy types. In Section 4, we discuss the results of our investigation including those on the purity and completeness of traditional K+A selection and the differences between galaxies selected using traditional means and those selected with our observations. Finally, in Section 5 we summarize all of our results. Throughout this paper all magnitudes, including those in the IR, are presented in the AB system (Oke & Gunn 1983; Fukugita et al. 1996). All EW measurements are presented in the rest frame and we adopt the convention of negative EWs corresponding to a feature observed in emission. All distances are quoted in proper units. We adopt a concordance ΛCDM cosmology with $H_0 = 70$ km s^{-1} Mpc^{-1}, $\Omega_\Lambda = 0.73$, and $\Omega_M = 0.27$.

2 TARGETS AND OBSERVATIONS

The subject of this study is the galaxy population in and surrounding two LSSs at $z \sim 0.8$, SG0023 and RXJ1716, drawn from the Observations of Redshift Evolution in Large Scale Environments (ORELSE; Lubin et al. 2009) survey. The ORELSE survey is a massive ongoing photometric and spectroscopic campaign dedicated to mapping out and characterizing the galaxy population in and around ∼20 LSSs at $0.6 \leq z \leq 1.3$. These two LSSs were chosen from the full ORELSE sample to be the maiden fields for MOSFIRE observations due to (a) their similarity in redshift, (b) their similar extensive coverage in optical/NIR imaging and optical spectroscopy, (c) their encompassing the full range of properties of LSSs targeted by the ORELSE survey at these redshifts and (d) falling at a redshift where the Hα λ6563 Å and the [N II] λ6583 Å features are comfortably situated away from bright OH lines in the *J*-band sky. The optically selected SG0023 supergroup at $z \sim 0.83$ is composed of at least five distinct groups ($\sigma_v < 550$ km s^{-1}) characterized by relatively low dynamical masses ($\log(\mathcal{M}_{\rm vir}/\mathcal{M}_\odot) = 12.7 - 13.9$), a lack of discernible diffuse X-ray emission originating from a hot medium (Rumbaugh et al. 2013), and a galaxy population primarily composed of star-forming and starbursting galaxies (Lubin et al. 2009). In stark contrast, the massive ($\log(\mathcal{M}_{\rm vir}/\mathcal{M}_\odot) = 15.2$), X-ray selected RXJ1716 cluster at $z \sim 0.81$ is characterized by a strong, regular diffuse intracluster medium (ICM) emission ($L_{X,\,\rm bol} = 9.3 \pm 0.4 \times 10^{44}$ ergs s^{-1}; Vikhlinin et al. 2002; Rumbaugh et al. 2017), though with low-level, but significant, structure near its outskirts, a core of massive ($\log(\mathcal{M}_*/\mathcal{M}_\odot) > 11$), quiescent members, and a large overall fraction of quiescent member galaxies[2] (∼50 per cent) to the stellar mass completeness limit of the spectroscopic survey ($\log(\mathcal{M}_*/\mathcal{M}_\odot) \geq 10$). However, despite what appears to be an evolved, isolated structure, the LSS appears to house appreciable spatial and velocity sub-structure and estimates of its halo mass from lensing (Clowe et al. 1998) and X-ray (Ettori et al. 2004) ($3 - 4 \pm 1 \times 10^{14}$ $\mathcal{M}_\odot$) are both considerably below the estimate made from the dynamics of its member population (see Table 1), indicating at least a moderate departure from virialization. The general properties of the member groups and cluster of the two LSSs are given in Table 1. In this section we briefly discuss the imaging and spectroscopic data taken of these LSSs and their surrounding fields.

2.1 Imaging and photometry

The wealth of imaging data available as well as their depth for both SG0023 and RXJ1716 is given in Table 2. Here we briefly summarize the observations and reduction of these data. A full description of the reduction process of these data will be given in Tomczak et al. (submitted). Optical imaging of the two LSSs was taken from our own observations with the Large Format Camera (LFC; Simcoe et al. 2000) on the Palomar 5-m telescope and our own and archival imaging with Suprime-Cam (Miyazaki et al. 2002) mounted on the Subaru 8-m telescope. Reduction of the LFC data was done in the Image Reduction and Analysis Facility (IRAF; Tody 1993) and follows the methods outlined in Gal et al. (2008). Reduction of the Suprime-Cam data was performed with the SDFRED2 pipeline (Ouchi et al. 2004) supplemented by several Traitement Élémentaire Réduction et Analyse des PIXels (TERAPIX[3]) routines. Photometric calibration in all cases was performed from observations of Landolt (1992) standard star fields taken on the same night of each observation.

NIR imaging in the *J* and *K* bands was taken with the Wide-Field Camera (WFCAM; Casali et al. 2007) mounted on the United Kingdom Infrared Telescope (UKIRT) and the Wide-field InfraRed Camera (WIRCam; Puget et al. 2004) mounted on the Canada–France–Hawai'i Telescope (CFHT) for SG0023 and

[2] When referring to a particular cluster or group, the definition of a 'member galaxy is given in Table 1. For LSSs, a member galaxy is defined more loosely as simply a galaxy in the redshift range of that LSS within the spatial constraints of our DEIMOS coverage.
[3] http://terapix.iap.fr

Table 1. Cluster and group properties.

Structure	α^a_{J2000} [deg]	δ^a_{J2000} [deg]	$\langle z \rangle$	$N^b_{\rm mem,spec}$	σ^c_v [km s^{-1}]	$M_{\rm vir}$ [log $\mathcal{M}_\odot$]
RXJ1716	259.2016	67.1392	0.8116	144	1150 ± 162	15.2 ± 0.2
SG0023A	6.0256	4.3590	0.8396	29	507 ± 126	13.8 ± 0.6
SG0023B1	5.9757	4.3884	0.8290	11	106 ± 51	12.7 ± 0.3
SG0023B2	5.9697	4.3820	0.8453	17	231 ± 54	13.3 ± 0.3
SG0023C	5.9247	4.3807	0.8466	70	544 ± 59	13.7 ± 0.3
SG0023M	5.9674	4.3199	0.8472	17	487 ± 85	13.9 ± 0.3

Notes. [a]: I^+/i'-luminosity-weighted centre of member galaxies calculated using the method described in Ascaso et al. (2014). [b]: Defined as galaxies with $|\Delta_v| \leq 3\sigma_v$ from $\langle z \rangle$ and $R_{\rm proj} < 2R_{\rm vir}$ from the optical spatial centre, except for SG0023B1/B2 where coherent structure in differential velocity was observed out to $R \gg R_{\rm vir}$, for which we adopted $R_{\rm proj} \leq 0.5\ h_{70}^{-1}$ Mpc. [c]: The measured line-of-sight (LOS) galaxy velocity dispersion measured using the method of Lemaux et al. (2012).

Table 2. Imaging data.

Band	Telescope/instrument	Depth[a]
RXJ1716		
B	Subaru/Suprime-Cam	25.5
V	Subaru/Suprime-Cam	26.0
R_C	Subaru/Suprime-Cam	25.8
I^+	Subaru/Suprime-Cam	25.1
Z^+	Subaru/Suprime-Cam	24.3
J	CFHT/WIRCam	21.9
K_s	CFHT/WIRCam	22.3
[3.6]	*Spitzer*/IRAC	22.5
[4.5]	*Spitzer*/IRAC	22.1
[5.8]	*Spitzer*/IRAC	21.6
[8.0]	*Spitzer*/IRAC	20.6
SG0023		
B	Subaru/Suprime-Cam	26.4
V	Subaru/Suprime-Cam	25.9
R^+	Subaru/Suprime-Cam	25.2
r'	Palomar/LFC	25.1
I^+	Subaru/Suprime-Cam	24.6
i'	Palomar/LFC	24.5
z'	Palomar/LFC	23.1
J	UKIRT/WFCAM	22.0
K	UKIRT/WFCAM	22.0
[3.6]	*Spitzer*/IRAC	22.2
[4.5]	*Spitzer*/IRAC	21.9

Note. [a]5σ point source completeness limit.

RXJ1716, respectively. The UKIRT data were processed using the standard UKIRT processing pipeline courtesy of the Cambridge Astronomy Survey Unit[4] and the CFHT data through the I'iwi pre-processing routines and TERAPIX. The photometric calibration of the mosaics output by both pipelines was done selecting bright ($m < 15$), non-saturated objects with existing Two Micron All Sky Survey (2MASS; Skrutskie et al. 2006) photometry. Further infrared imaging was obtained with the *Spitzer* (Werner et al. 2004) InfraRed Array Camera (IRAC; Fazio et al. 2004) in all four channels for RXJ1716 and the two non-cryogenic channels ([3.6]/[4.5]) for SG0023. The basic calibrated data (cBCD) images provided by the *Spitzer* Heritage Archive were reduced using the MOsaicker and Point source EXtractor (MOPEX; Makovoz & Marleau 2005) package in conjunction with several custom Interactive Data Language (IDL) scripts written by J. Surace. Further details are given in Tomczak et al. (submitted). All *Spitzer* imaging is provided flux-calibrated in units of MJy/sr.

For the ground-based imaging, photometry was obtained by running Source Extractor (SExtractor; Bertin & Arnouts 1996) in dual-image mode using an inverse-variance-weighted R^+I^+ and $R_CI^+Z^+$ stack as the detection image for SG0023 and RXJ1716, respectively. Prior to running SExtractor in each field, all images are registered to a common grid and convolved to the worst point spread function (PSF) for that field (1 and 0.9 arcsec for SG0023 and RXJ1716, respectively) estimated from stacked point sources in each image using the Richardson & Lucy algorithm in `scikit-image` to generate the convolution kernel. Fixed aperture photometry (1.3× the FWHM of the homogenized PSF) was then performed on these PSF-matched images ensuring that an identical fraction of the light of each object is measured in all broad-band images. An aperture correction was made to the measured magnitudes by scaling the ratio of aperture and AUTO flux densities as measured in the detection image, a similar practice to that commonly adopted in other large surveys (e.g. Laigle et al. 2016; Moutard et al. 2016). Magnitude uncertainties were calculated from adding, in quadrature, SExtractor uncertainties to our own estimates of background noise drawn from the 1σ root-mean-square (RMS) scatter of measurements in hundreds of blank sky regions for each band. Photometry for the *Spitzer*/IRAC images was treated separately due to the appreciably larger and differently shaped PSF (∼2 arcsec) in these bands relative to the ground-based images. The package T-PHOT (Merlin et al. 2015) was used to translate the segmentation map in the detection image for each field to its equivalent in the *Spitzer*/IRAC images using a given kernel and to mitigate blending through optimal scaling of the resultant convolved segmentation map estimated from a fit to the observed data. Flux densities are then extracted from the scaled best-fitting model of each object. A summary of all imaging data and associated depths for both fields is given in Table 2.

2.2 Optical spectroscopy

Imaging in the $r'i'z'$ from LFC and $R_CI^+Z^+$ from Suprime-Cam was used to select spectroscopic targets in the SG0023 and RXJ1716 fields, respectively, following the methods outlined in Lubin et al. (2009). Briefly, the two unique colours provided by the three observed bands were used to prioritize spectroscopic targets, with the highest priority targets corresponding to galaxies with colours closest to the expected colours of quiescent galaxies at $z \sim 0.8$ (see table 2 of Lubin et al. 2009). Objects with colours with progressively larger deviations from the colour range that defined the highest priority targets were assigned progressively lower priorities.

[4] http://casu.ast.cam.ac.uk/surveys-projects/wfcam/technical

Table 3. MOSFIRE targets in the SG0023 and RXJ1716 fields.

Sample[a,b]	$N_{\rm DEIMOS}$	$N_{\rm targeted}$	$N_{\rm KAIROS}$	$N_{\rm K+A\text{-}H\alpha}$
Priority I: Traditional K+A	40 (29)	20 (19)	–[c]	15 (14)
Priority II: Starburst/KAIROS	188 (118)	69 (60)	15 (12)	–[c]
Priority III: Star forming	178 (119)	32 (31)	–[c]	–[c]
Quiescent	113 (82)	15 (14)	–[c]	–[c]

Notes. [a]Numbers given are for SG0023 and RXJ1716 combined and for galaxies in the redshift range $0.775 \leq z \leq 0.912$ (see Section 2.3).
[b]Numbers in parentheses refer to LSS members galaxies only.
[c]Not possible by definition.

While galaxies were prioritized in such a way, due to the relative scarcity of the highest priority objects on the sky, the vast majority of spectroscopic targets in both fields (∼80 per cent) were objects with colours that deviated from those expected from $z \sim 0.8$ quiescent galaxies. Observed-frame optical spectroscopy was performed with the DEep Imaging and Multi-Object Spectrometer (DEIMOS; Faber et al. 2003) at the Naysmith focus of the Keck II telescope. All DEIMOS observations were performed using the 1200 l mm^{-1} grating with slitmasks employing 1 arcsec wide slits and the grism tilted to a λ_c between 7500 and 7800 Å. This setup resulted a plate scale of 0.33 Å pix^{-1}, an $R \sim 5000$ ($\lambda/\theta_{\rm FWHM}$, where $\theta_{\rm FWHM}$ is the full-width half-maximum resolution), and a wavelength coverage of $\Delta\lambda \sim 2600$ Å. Spectroscopic targets were generally limited to $i'/I^+ < 24.5$ with a tail extending to $i'/I^+ \sim 25.5$.

In the SG0023 field, nine DEIMOS masks were observed between September 2005 and September 2010 under photometric conditions with seeing that ranged from 0.45 to 0.81 arcsec. Integration times per mask ranged from 5700s and 9400s, with $\tau_{\rm int}$ scaled to roughly achieve a uniform distribution of continuum S/N per resolution element across all masks independent of both conditions (in this case seeing only) and the i' distribution of target objects. Data were reduced using a modified version of the Deep Evolutionary Extragalactic Probe 2 (DEEP2; Davis et al. 2003; Newman et al. 2013) SPEC2D pipeline. All objects, those targeted and those which serendipitously fell in a slit, were visually inspected and assigned a spectroscopic redshift (hereafter $z_{\rm spec}$) and a redshift quality code (Q) in the `zspec` environment (see Newman et al. 2013). A total of 1081 unique objects were targeted and/or detected, which resulted in 943 high-Q $z_{\rm spec}$ measurements ($Q = -1$, 3, 4; see Gal et al. 2008; Newman et al. 2013, for the meaning of these values) of which 213 are in the adopted redshift range of the supergroup, $0.820 \leq z \leq 0.855$.

In the RXJ1716 field, six DEIMOS masks were observed between September 2010 and May 2015 with the grating tilted to $\lambda_c = 7800$ Å for all masks. Exposure times ranged from 5400s to 9000s under seeing that ranged from 0.54 to 0.83 arcsec and conditions that ranged from light cirrus to photometric. A total of 828 unique objects were targeted and/or detected, which resulted in 571 high-Q $z_{\rm spec}$ measurements of which 144 are in the adopted cluster redshift range $0.798 \leq z \leq 0.826$. These observations are sufficiently deep to determine continuum redshifts consistently to $I^+ \leq 23.5 - 24$ or roughly $0.4L^*$ at $z \sim 0.8$[5] with secure redshifts based on emission line features obtainable to the limiting magnitude of the DEIMOS survey ($I^+ \sim 25.5$).

Equivalent widths (EWs) measurements of the [O II] λ3726,3279 Å doublet and the Hδ λ4101 Å Balmer series line were performed following the bandpass method described in Lemaux et al. (2010) on all high-Q extragalactic spectra where the wavelength coverage allowed for the possibility of the features to be present. All measurements were visually inspected and bandpasses were tweaked when obvious reduction artefacts were present. These measurements would serve as the basis for the Multi-Object Spectrometer For Infra-Red Exploration (MOSFIRE; McLean et al. 2012) campaign that followed.

2.3 Near-infrared spectroscopy

The DEIMOS EW measurements for galaxies within the redshift ranges $0.775 < z < 0.912$ and $0.975 < z < 1.020$ were used to select targets for follow-up NIR J-band spectroscopy with MOSFIRE. These redshift ranges were chosen so that [O II] and Hδ are almost certain to fall within the wavelength coverage of DEIMOS for all slits[6] and that both the Hα λ6563 Å and the [N II] λ6583 Å features fall within the wavelength coverage of the MOSFIRE J-band spectroscopy ($1.150 \leq \lambda \leq 1.350$ μm) away from the strongest OH features in the J-band sky ($1.260 \lesssim \lambda \lesssim 1.295$μm). From these measurements, three main classes of MOSFIRE targets were formed. In order of priority, these were (I) K+A [EW([O II]) > −3 Å, EW(Hδ) >4 Å and, visually, the absence of Hβ emission when the spectral coverage allowed for it], (II) starbursts [EW([O II]) < −3 Å, EW(Hδ) >4 Å], and (III) star-forming galaxies [EW([O II]) < −3 Å, EW(Hδ) <4 Å]. Quiescent galaxies [EW([O II])>-3 Å, EW(Hδ) <4 Å] were generally avoided as MOSFIRE targets.

Such a scheme is largely consistent with those employed by other K+A studies at $z \sim 1$ (see the review of the logic behind a similar classification scheme in Poggianti et al. 2009). Additionally, this metric of classification shows a high degree of congruence with classification that uses the observed-frame $R_C - I^+$ and $R^+ - I^+$ colours. For example, in RXJ1716 and SG0023, spectroscopically classified quiescent galaxies exhibit, by far, the reddest median colours (1.05 and 1.33, respectively), are the most massive in terms of their stellar content ($\langle \log(\mathcal{M}_*/\mathcal{M}_\odot) \rangle = 10.67$ and 10.79, respectively), and have the highest incidence (87 per cent and 80 per cent, respectively) of galaxies with colours consistent with the cluster/group red sequences as measured by the methods defined in Lemaux et al. (2012) (see Fig. 1). The EW([O II]) threshold adopted here was set by fitting a half Gaussian to the positive portion of the distribution of EW([O II]) for all galaxies in the RXJ1716 and SG0023 field

[5] L* is adopted from De Propris, Phillipps & Bremer (2013) for $z = 0.6$ cluster galaxies and translated to the redshift and filter of interest using EZGal, http://www.baryons.org/ezgal/

[6] Variations of up to ∼±120 Å in λ_c can occur depending on the placement of slit on the slitmask along the direction parallel with the dispersion direction meaning, in some cases, we did not have the coverage to detect one of the two features.

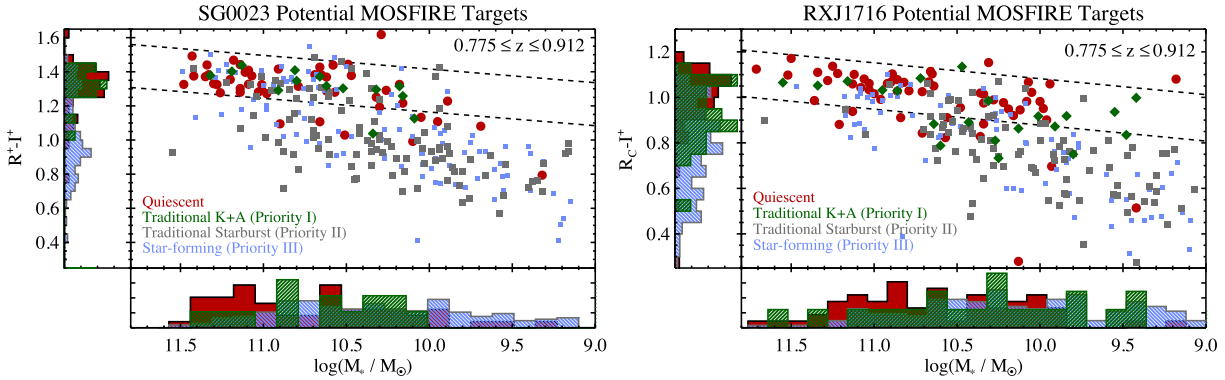

Figure 1. Left: Observed-frame $R^+ - I^+$ colour-stellar mass (CSMD) for potential MOSFIRE target galaxies in the SG0023 field in the lower of the two target redshift ranges ($0.775 < z < 0.912$). Only this redshift range is plotted as this is the redshift range adopted for all subsequent analysis presented in this study. All galaxies shown in this plot have a secure spectroscopic redshift and measurements of EW([O II]) and EW(H δ). Galaxies are classed into quiescent (red circles), K+A (green diamonds), starburst (grey squares) and star-forming (light blue squares) galaxies using traditional methods based on the strength of the [O II] and H δ features. Dashed lines indicate the bounds of the red sequence. Area normalized histograms are plotted for quiescent (red filled), K+A (green hatched) and starburst+star-forming (grey/light blue hatched) galaxies for both stellar mass and colour. Right: Similar to the left-hand panel except the population plotted is that of the RXJ1716 field and the R^+ filter has been exchanged for the R_C filter. Galaxies in an identical redshift range as those in the left-hand panel are shown. In both SG0023 and RXJ1716 galaxies classified as quiescent are generally redder and more massive in their stellar content than any of the other spectral classes. K+A galaxies appear to be intermediate to the quiescent and star-forming/starbursting classes in terms of both stellar mass and observed-frame colour.

where this quantity was measured (i.e. where [O II] is observed to be in absorption). As such values are unphysical, this part of the distribution results purely from noise (instrumental or astrophysical). The threshold of EW([O II]) $= -3$ Å was chosen as it is 1.5σ of the resultant half-Gaussian fit, which, with 144 such galaxies in our sample, implies that $\leq$10 galaxies with spuriously detected [O II] emission contaminate our star-forming and starbursting samples (i.e. $>1.5\sigma$ on the negative side of the distribution). The true number is likely less as each [O II] feature is visually inspected in the 1d and 2d DEIMOS spectra. The H δ cut adopted here for K+A populations is a compromise between those chosen by various other studies (Zabludoff et al. 1996; Balogh et al. 1999; Dressler et al. 1999; Bartholomew et al. 2001; Le Borgne et al. 2006; Poggianti et al. 2009; Swinbank et al. 2012) and, in conjunction with the cut on [O II], ensures, at least to the ability of the DEIMOS data to discriminate that the last major star-formation event ended within $\lesssim$1.5 Gyr irrespective of SFH (see e.g. discussion in Poggianti et al. 1999). While this may seem like an excessively long time-scale constraint to use to select a transition population, this time-scale is less ($\leq$1 Gyr) in both synthetic models (e.g. Lemaux et al. 2012) and hydrodynamic simulations (e.g. Snyder et al. 2011) when only considering SFHs that include, at some point during the history of a galaxy, a starburst. Such starbursts need not be strong, it is sufficient that they form $\sim$5–10 per cent of the stellar mass of the galaxy in the event, and, indeed, it is suggested that a starburst of at least this modest level is necessary to form K+A features (e.g. Balogh et al. 2005; Wild et al. 2009; Melnick & De Propris 2013, though see e.g. Newberry, Boroson & Kirshner 1990; Poggianti et al. 1999; Le Borgne et al. 2006; Falkenberg, Kotulla & Fritze 2009; Yan et al. 2009, for an alternate view). However, a similarly tight age constraint also applies if K+A features are produced through rapidly quenched normal (or bursty) star formation (Yan et al. 2009) making the distinction largely superfluous for this study. We will show later (see Section 4.2) that this cut selects K+A galaxies that have, on average, ended their star formation within $\lesssim$1 Gyr. There were 194 (24/93/77) and 257 (23/123/111) potential MOSFIRE targets of these three main classes in RXJ1716 and SG0023, respectively, bounded by the quoted redshift ranges, where values inside the parentheses indicate the number of priority I, II, and III targets, respectively.

Three masks in RXJ1716 and three masks in SG0023 were observed on 2014 August 15 with MOSFIRE under photometric conditions with seeing ranging from 0.5 to 0.9 arcsec. Integration time for all masks was $7 \times 4 \times 120$s (3360s), with an ABBA nod pattern employed for each block of 4×120s exposures nod pattern. Slit widths were set to 0.7 arcsec and the plate scale to 1.3 Å pix^{-1} resulting in an $R \sim 3500$. The *python*-based `MOSFIRE DRP`[7] was used to reduce the raw frames. This pipeline provides dark-subtracted, flat-fielded, rectified, wavelength-calibrated, background-subtracted two-dimensional flux density and variance arrays for every slit. Each two-dimensional flux density spectrum output by the pipeline was collapsed along the dispersion axis and a Gaussian iteratively fit to the resulting collapsed profile with a mean location beginning with the expected spatial location of the targeted galaxy. The final parameters of the Gaussian fit, mean and $\pm1.5\sigma$, set the limits on the boxcar extraction used to generate the one-dimensional flux density and noise spectrum. In cases where the continuum was marginally detected in MOSFIRE or only emission lines were present, the dispersion axis would be collapsed over a limited wavelength range and the fit was done by hand. During this process it was noticed that the error arrays output by the pipeline (i.e. the square root of the variance arrays) appeared to be discordant with the RMS of the observed spectra away from bright OH lines in that the former appeared to overestimate the true noise present in the data.[8] In an attempt to rectify this discrepancy, all error spectra were scaled by the ratio of the RMS to the median error for that spectrum (roughly a factor of 4 in all cases). Absolute spectrophotometric calibration was performed by observations of standards throughout the night, though, in practice, this step was largely superfluous as we focus in this study almost exclusively on relative quantities.

[7] http://www2.keck.hawaii.edu/inst/mosfire/drp.html

[8] This was a known issue in the earlier version of the pipeline employed for our data. According to the official documentation, there no longer remains issues with the output variance arrays for the newest version of the pipeline.

In total, 78 galaxies were observed with MOSFIRE in each of the two fields to an average 3σ line limit of $f_{\rm line} \geq 7 \times 10^{-18}$ ergs s^{-1} cm^{-2}, including a slit loss correction appropriate for the average targeted galaxy, equivalent, for Hα, to an unobscured SFR of $\sim$0.1 M$_\odot$ yr^{-1} at $z = 0.83$ adopting the conversion of Kennicutt (1998) and scaling to a Chabrier (2003) initial mass function (IMF). Of these 156 galaxies, 61 (12/36/13) and 65 (8/37/20) in RXJ1716 and SG0023, respectively, were composed of the three main classes described above and fell within the redshift ranges adopted earlier in this section ($0.775 < z < 0.912$ and $0.975 < z < 1.020$). The remaining 17 and 13 MOSFIRE targets in RXJ1716 and SG0023, respectively, were at different redshifts, were spectrally classed as quiescent, or were $z_{\rm phot}$ members with no corresponding DEIMOS spectra and thus excluded from the remainder of our analysis. The above numbers for the three main classes result in a 42.6 per cent, 32.0 per cent, and 17.5 per cent MOSFIRE targeting completeness for K+As, starbursts, and star-forming galaxies, respectively, across the redshift ranges of interest. As only a small number of priority I, II and III galaxies were observed across the two fields in the higher redshift bin (i.e. four priority II targets), in this paper we will focus exclusively on the lower redshift bin for which the MOSFIRE targeting completeness was higher, 50.0 per cent, 36.7 per cent, and 18.0 per cent for priority I, II and III galaxies, respectively. This redshift range contains the vast majority ($\sim$95 per cent) of galaxies targeted with MOSFIRE across the two fields, is roughly centred at the redshift range of the two LSSs, and retains a large number of both DEIMOS- and MOSFIRE-targeted galaxies while not appreciably compromising completeness. While some portions of the galaxies in this redshift range are found in the coeval field, a majority ($\sim$70 per cent) are members of the two LSSs. Line flux measurements were made following the bandpass method of Lemaux et al. (2010) with 3σ upper limits imposed on any line not significantly detected. Because the MOSFIRE observations did not generally go to sufficient depth to significantly detect stellar continua, the Hα emission line flux (or limits thereon) calculated after applying a slit loss correction was used in conjunction with the J-band magnitudes, transformed to the rest-frame, to calculate EW(Hα).

3 METHODS

3.1 Broadband spectral energy distribution fitting

Spectral energy distribution (SED) fitting was performed on the imaging in three stages. First, aperture magnitudes were input to the code Easy and Accurate $z_{\rm phot}$ from Yale (EAZY; Brammer, van Dokkum & Coppi 2008) for the purposes of estimating photometric redshifts (hereafter $z_{\rm phot}$). For each object, the $z_{\rm phot}$ is estimated from a probability distribution function (PDF) generated by minimizing the χ^2 of the observed flux densities and a set of seven basis templates at each redshift. These seven basis templates were generated from a large library of PEGASE models (Fioc & Rocca-Volmerange 1997; see also Grazian et al. 2006) following the methodology given in section 2.2 of Brammer et al. (2008), though several changes in the input models were made since this time including the implementation of emission lines (Brammer et al. 2011). The parameter '$z_{\rm peak}$' was adopted as the measure of $z_{\rm phot}$, with the uncertainties on this parameter estimated from the PDF of each source. Also at this stage, a second round of fitting was performed separately for which we exclusively employed stellar templates drawn from the Pickles (1998) library. The reduced χ^2 values between the two sets of fits were compared to separate, in conjunction with other criteria, stars from galaxies. A use flag was generated for all objects in the photometric catalogue that allowed for the removal of those objects that were likely stellar, had an S/N < 3 in the detection band, were covered in less than five of the broad-band images, had significant saturation (>20 per cent of the segmentation map pixels), or were poorly fit in the galaxy portion of the SED fitting (see Straatman et al. in preparation). Such objects totaled $\sim$4 and $\sim$9 per cent of the photometric objects in the SG0023 and RXJ1716 fields, respectively, over the area bounded by the DEIMOS coverage. These objects were removed from our analysis.

The precision and accuracy of the photometric redshifts were estimated from fitting a Gaussian to the distribution of $(z_{\rm spec} - z_{\rm phot})/(1 + z_{\rm spec})$ measurements in the range $0.5 \leq z \leq 1.2$ and was found to be $\sigma_{\Delta z/(1+z)} = 0.025$ with a catastrophic outlier rate ($\Delta z/(1 + z) > 0.15$) of $\eta \sim 4$ per cent for both fields to a limit of $I^+ \leq 24.5$. At this point, a slight systematic offset from zero ($\Delta z/(1 + z_{\rm phot}) \sim 0.01$) was noticed for both fields. The value of this offset, multiplied by $(1+z_{\rm phot})$, was applied to all raw $z_{\rm phot}$ values. The spectroscopic sample was also used during the initial fitting to iteratively correct the photometric zero-points of each filter following the methodology of Brammer et al. (2011). These corrections assume that the properties and statistics of the spectroscopic sample, a sample that constitutes only 1.4–2.8 per cent of the usable photometric objects in the region bounded by the DEIMOS coverage, can be applied to the underlying photometric sample. For the single facet of this analysis where we rely at all on $z_{\rm phot}$ measurements (Section 3.2), we cut the photometric sample in a magnitude range matched to the spectroscopic sample such that this assumption likely holds.

For the second stage of the SED fitting process, the EAZY code is again run, but this time setting either the high-Q $z_{\rm spec}$, when available, or the $z_{\rm phot}$ from EAZY as a redshift prior. Identical models are employed at this stage as were employed at the first stage. Identical photometric zero-points are also applied. At the conclusion of this fitting, rest-frame magnitudes are directly estimated from the best-fitting template following the methodology of Brammer et al. (2011). These extinction-uncorrected rest-frame aperture magnitudes are corrected to total magnitudes by the scaling method described in Section 2.1.

For the final stage of the fitting process, the code Fitting and Assessment of Synthetic Templates (FAST; Kriek et al. 2009) was used to perform SED fitting on the aperture-corrected magnitudes using the same redshift priors as were used in the second stage, again with identical photometric zero-points applied. Exponentially declining stellar population synthesis Bruzual & Charlot 2003 models (hereafter BC03) were adopted with a Chabrier 2003 IMF and a Calzetti et al. (2000) extinction law. The ranges of allowed parameters are comparable to those of Tomczak (in preparation). For each fit, the maximum age is bounded by the age of the universe at the $z_{\rm spec}$ or $z_{\rm phot}$ redshift. Stellar-phase metallicity was fixed to $Z = Z_\odot$. For this paper only stellar masses derived from this fitting are used. Each parameter is estimated from the best-fitting value, and uncertainties are derived through 100 realizations of re-fitting to an SED with photometry that has been tweaked by a Gaussian random multiple of its photometric errors for each band (as in e.g. Ryan et al. 2014).

3.2 Local overdensity

For certain aspects of this analysis we will focus on the environmental distribution of various types of galaxies. While environmentally driven evolution within LSSs is certainly a complex function of redshift, smaller-scale galaxy density, and the properties of the LSS in which a galaxy resides, we choose in this paper to focus

almost exclusively on local overdensity as a proxy for environment. In future studies that will include all ORELSE fields, this analysis will extend to separately binning the distribution of different classes of galaxies varying local density, halo mass, dynamical and spatial distribution within the LSS, and redshift while holding the other quantities fixed. In order to estimate the local environment of the galaxies in our sample, we employ the Voronoi Monte Carlo technique described in Lemaux et al. (2017a). The method that we employ broadly follows that employed in Darvish et al. (2015), in which it was found, through comparisons to simulated density fields, that the 'weighted Voronoi tessellation estimator' computed in that study matched or exceeded the accuracy and precision of all other metrics of density estimation. The one metric with comparable performance to the Voronoi approach, weighted adaptive kernel estimation, is sensitive to both the form and size of the kernel and, generally, employs a spatially symmetric kernel (along the transverse dimensions) that is not ideal for the complex LSSs studied here. Further quantitative measures of the accuracy and precision of our implementation derived from (over)density field reconstructions on mock catalogs will be described in Tomczak et al. (2017) and Lemaux et al. (2017b). We discuss the version of Voronoi Monte Carlo technique employed here briefly.

For each Monte Carlo realization, Gaussian sampling is performed for each object without a high quality $z_{\rm spec}$ (but with a good use flag; see Section 3.1). The sampled value, in units of σ, is then multiplied by either the effective 1σ lower or upper uncertainty on $z_{\rm phot}$ for that object depending on which side of the peak of the Gaussian sample it fell. For each object, this value is then either subtracted from or added to its original $z_{\rm phot}$ to create a new $z_{{\rm phot},\ MC_i}$ for that realization. These objects, along with all galaxies with high-quality extragalactic $z_{\rm spec}$, are sliced into 85 redshift bins running from $0.55 \leq z \leq 1.4$, and Voronoi tessellation is performed on each realization of redshift slice on all objects that fall within that redshift bin. For each realization of each slice, a grid of 75×75 kpc is created to sample the underlying local density distribution. The local density at each grid value for each realization and slice is set equal to the inverse of the Voronoi cell area (multiplied by D_A^2) of the cell that encloses the central point of that grid. Final local densities, $\Sigma_{\rm VMC}$, for each grid point in each redshift slice are then computed by median combining the values of 100 realizations of the Voronoi maps for that slice. The local overdensity value for each grid point is then computed as $\log(1+\delta_{\rm gal}) \equiv \log(1+(\Sigma_{\rm VMC}-\tilde{\Sigma}_{\rm VMC})/\tilde{\Sigma}_{\rm VMC})$, where $\tilde{\Sigma}_{\rm VMC}$ is the median $\Sigma_{\rm VMC}$ for all grid points over which the map is defined (i.e. where there is coverage in a sufficient number of bands). By adopting local overdensity rather than local density as a proxy of evironment, we largely mitigate issues of sample selection and differential bias as a function of redshift.

Two main changes were made with respect to the method detailed in Lemaux et al. (2017a) to adapt this technique to the ORELSE data. The first is that redshift slices were defined not to be constant in line of sight proper distance but rather in velocity space encompassing ± 1500 km s^{-1} from the central redshift of each bin. This velocity width was imposed to roughly match the average $\pm 3\sigma_v$ of the constituent sub-structures of the LSSs presented in this paper and ranges from $\pm 1.3\sigma_v$ to $\pm 14.2\sigma_v$ for individual sub-structures (see Table 1). The second change made was to treat $z_{\rm spec}$ measurements in a binary fashion in that galaxies with high-Q $z_{\rm spec}$ measurements always had their redshifts fixed to $z_{\rm spec}$ rather than have some chance in each realization of being treated in the probabilistic manner described above. Voronoi Monte Carlo maps were generated in half steps of 1500 km s^{-1} with central redshift bins running from $0.55 \leq z \leq 1.4$. For all Voronoi Monte Carlo maps, the photometric and spectroscopic catalogues were cut at $18 \leq I^+ \leq 24.5$, a magnitude range that encompasses nearly all high-Q ORELSE objects. For the redshift slices used in this study ($0.775 \leq z \leq 0.912$; see Section 2.3), the median fraction of $z_{\rm spec}$ to $z_{\rm phot}$ objects for all realizations across the entire area over which the maps were defined ($\sim 0.25^\circ$) varies from 3 to 37 per cent across the two fields, with a similar distribution in each field. Fig. 2 shows example slices of the Voronoi Monte Carlo maps centred at the average systemic

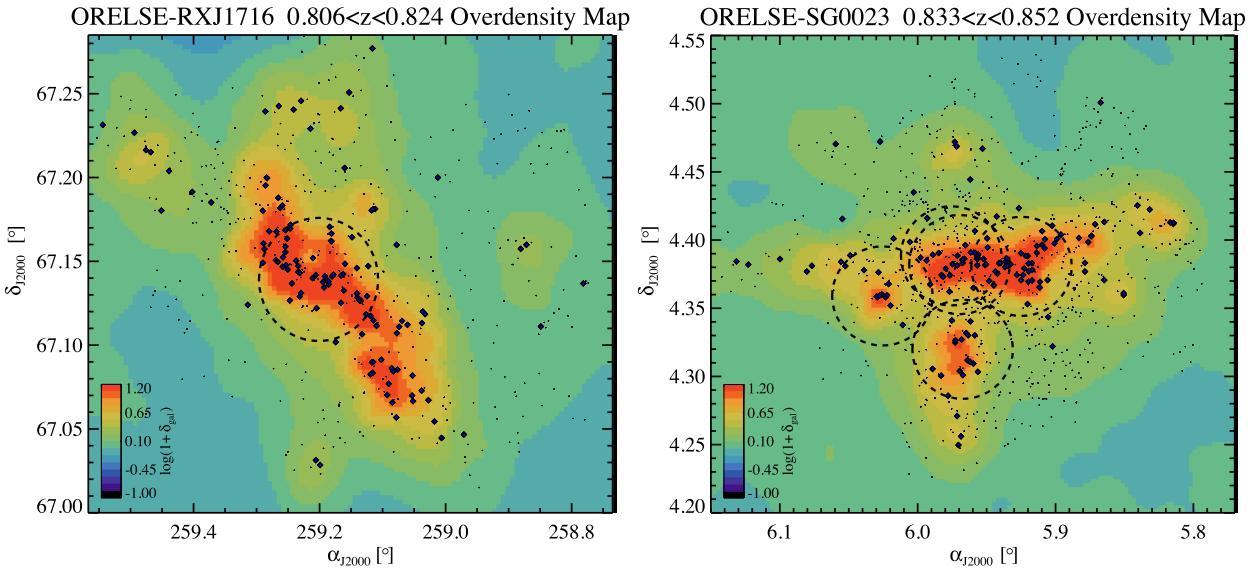

Figure 2. Voronoi Monte Carlo overdensity maps (see Section 3.2) of one redshift slice containing part (along the line of sight) of the RXJ1716 cluster (left) and the SG0023 supergroup (right). Redshift slices are bounded by ± 1500 km s^{-1} from the central redshift of each slice. The scale bar shown in the bottom left of each panel gives maps colours to their associated level of overdensity. Blue diamonds show the sky distribution of galaxies with high-quality spectroscopic redshifts that fall within the redshift range of each LSS (see Section 2.2), while small black points show that of all objects with high-quality spectroscopic redshifts. Dashed circles of radius $R_{\rm proj} = 1\ h_{70}^{-1}$ Mpc originating at the I^+/i' luminosity-weighted centres of the RXJ1716 cluster and five SG0023 member groups are overplotted. Only those objects with $18 \leq I^+ \leq 24.5$ were used to generate the maps. Both maps were smoothed by a Gaussian kernel with an FWHM of 4.5 pixels ($\sim 300\ h_{70}^{-1}$ kpc) for visualization purposes. Actual overdensity measurements are made on unsmoothed maps.

redshifts of SG0023 and RXJ1716. While the redshift slices shown in each panel of Fig. 2 do not span the entire redshift range of each LSS, it can be seen that the estimated density field largely traces the LSS members and peaks near the central regions of the constituent cluster and groups.

4 POST-STARBURST GALAXIES IN HIGH-REDSHIFT LARGE-SCALE STRUCTURES

With these observations and measurements in place, we now begin a preliminary census of the true K+A population in RXJ1716 and SG0023. In this study we focus our attention on two main aspects of this census. First, we investigate the incompleteness and impurity of K+A populations selected purely by observed-frame optical spectroscopy (e.g. DEIMOS) at $z \sim 1$ as revealed by our MOSFIRE observations and estimate the fraction of true K+A galaxies. Secondly, we investigate differences between the DEIMOS-selected K+A population and the true population of K+As in terms of their stacked broad-band properties and distribution across different environments.

4.1 Revealing the true post-starburst population

Using the traditional scheme to select post-starburst galaxies at high redshift, strong Balmer features, proxied by EW(H δ) > 4 Å, and the absence of emission lines traditionally associated with ongoing star formation, proxied by EW([O II]) > -3 Å (i.e. priority I galaxies; see Section 2.3), results in a K+A fraction of 7.7 ± 1.2 per cent (40/519). This fraction is calculated for all galaxies in our sample in the redshift range $0.775 \leq z \leq 0.912$ with $I^+ \leq 24.5$ for which a reliable EW(H δ) and EW([O II]) measurement could be made (see Section 2.3). The galaxies selected using this method will be referred to as 'traditional K+As' throughout the remainder of the paper. The fraction of traditional K+As does not change significantly if the redshift range is restricted to that of the two LSSs (8.3 ± 1.5 per cent, 29/348) and is broadly consistent with those found in other LSSs at similar redshifts (Tran et al. 2003, 2007; Poggianti et al. 2009; Muzzin et al. 2012; Wu et al. 2014). The former point is likely a reflection of the majority of the spectroscopic sample in our adopted redshift range being associated with the LSSs. This fraction also does not change significantly (7.7 ± 1.3 per cent, 31/405) if we instead calculate it after imposing the stellar mass limit of the spectroscopic sample (see Section 2). In a nearly equivalent exercise, we find that the traditional K+A fraction also remains statistically unchanged if we impose a stricter I^+-band cut, e.g. imposing $I^+ \leq 23.5$ results in a traditional K+A fraction of 6.9 ± 1.2 per cent (29/422).

As discussed in Section 2.3, with MOSFIRE we have targeted two populations that have the potential to be true K+A galaxies, defined as those galaxies with no ongoing star formation activity but which still fulfill our EW (H δ)>4 Å requirement. The first are the traditional K+As for which we have no evidence of ongoing star formation in our DEIMOS spectra (priority I galaxies). The second are the galaxies with K+A features that would have been classified as such but for the presence of formally significant [O II] emission (priority II galaxies). With the former we will attempt here to quantify the level of purity attained using the observed-frame optical selection, with the latter the level of completeness of this selection.

From the MOSFIRE observations of each galaxy we measured the flux ratio of the H α and [N II] emission features or placed limits thereon (see Section 2.3). This measure of (or limit on) the [N II]/H α is used in an attempt to determine the source of the emission for each galaxy. We classify those galaxies for which this ratio (or lower limit) is in excess of $\log([\mathrm{N\,II}]/\mathrm{H}\alpha) \geq -0.25$ as being *dominated* by emission from a process other than star formation, i.e. the emission originates from either that of a low-ionization nuclear emission-line region (LINER) or a Seyfert (hereafter LINER/Seyfert). This value was adopted as it excludes 100 per cent of galaxies within the SDSS star-forming locus (Kauffmann et al. 2003) as seen in the incarnation of the Baldwin, Phillips & Terlevich (1981) (hereafter BPT) diagram that employs [N II]. This [N II]/H α ratio is also higher than that exhibited by most SDSS composite objects and includes nearly all objects within the regions populated by LINERs and Seyferts (Kewley et al. 2006). While this classification scheme is calibrated for a galaxy sample at $z \sim 0.1$, little to no evolution is observed or predicted in various versions of the BPT diagram up to $z \sim 1$ (Kewley et al. 2013a,b; Jones, Martin & Cooper 2015). While systematically elevated [N II]/H α ratios have been observed for other star-forming populations observed with MOSFIRE (e.g. Sanders et al. 2015) such an offset may only apply to particular subsets of galaxies (Shapley et al. 2015) and are observed in samples appearing 4 Gyr earlier in cosmic time ($z \sim 2$) when physical conditions in star-forming galaxies appear to be appreciably different from those at lower redshift (see Sanders et al. 2015 and references therein). Such a cut also appears, from modelling, to be sufficient to select the vast majority of galaxies whose emission features are powered by both fast and slow shocks (Alatalo et al. 2016). Galaxies with an upper limit or a measured ratio below $\log([\mathrm{N\,II}]/\mathrm{H}\alpha) < -0.25$ we classify here as star forming. While the emission lines of such galaxies can still be partially powered by LINER/Seyfert emission, it is enough for our purposes that at least some of the emission can potentially come from star formation. In the left-hand panel of Fig. 3 we show EW([O II]) versus $\log([\mathrm{N\,II}]/\mathrm{H}\alpha)$ for all galaxies with EW(H δ)>4 Å that were targeted with MOSFIRE for which we measured a significant detection for at least [N II] or H α. In addition, we show the emission class of the galaxies when a definitive classification could be made. Traditional K+As are shown as galaxies with downward-facing arrows. The remaining galaxies are potential K+As that have [O II] emission significantly detected in their DEIMOS spectra (i.e. priority II galaxies). In the right-hand panel of Fig. 3 we plot the EW ratio of [O II] and H α versus $\log([\mathrm{N\,II}]/\mathrm{H}\alpha)$ for a subset of these galaxies (see Fig. 3 caption).

Of the 20 traditional K+As targeted with MOSFIRE for which we could make meaningful measurements, five exhibited significant ($>3\sigma$) H α emission in tandem with [N II]/H α ratios (or upper limits) consistent with originating from regions of ongoing star formation. Such galaxies are likely the product of heavy dust obscuration in which the [O II] (and potentially H β when it was possible to observe) is heavily differentially attenuated within H II regions strong enough to suppress even the EW([O II]) measurement, but from which appreciable numbers of H α photons can escape (see e.g. Oemler et al. 2009). As post-starburst galaxies cannot, by definition, house ongoing star formation, traditional classification of $z \sim 1$ K+A galaxies based solely on observed-frame optical spectroscopy results in a sample of 25 per cent contaminated by galaxies with active star formation. Such a fraction is statistically consistent with that seen in Wu et al. (2014) from a study of traditionally selected K+As in the SC1604 supercluster at $z \sim 0.9$ based on the prevalence of significant mid-infrared (MIR) emission. The remaining 15 galaxies for which either no H α emission was significantly detected or whose [N II]/H α ratios (or limits thereon) did not definitively point to star formation processes as the origin of

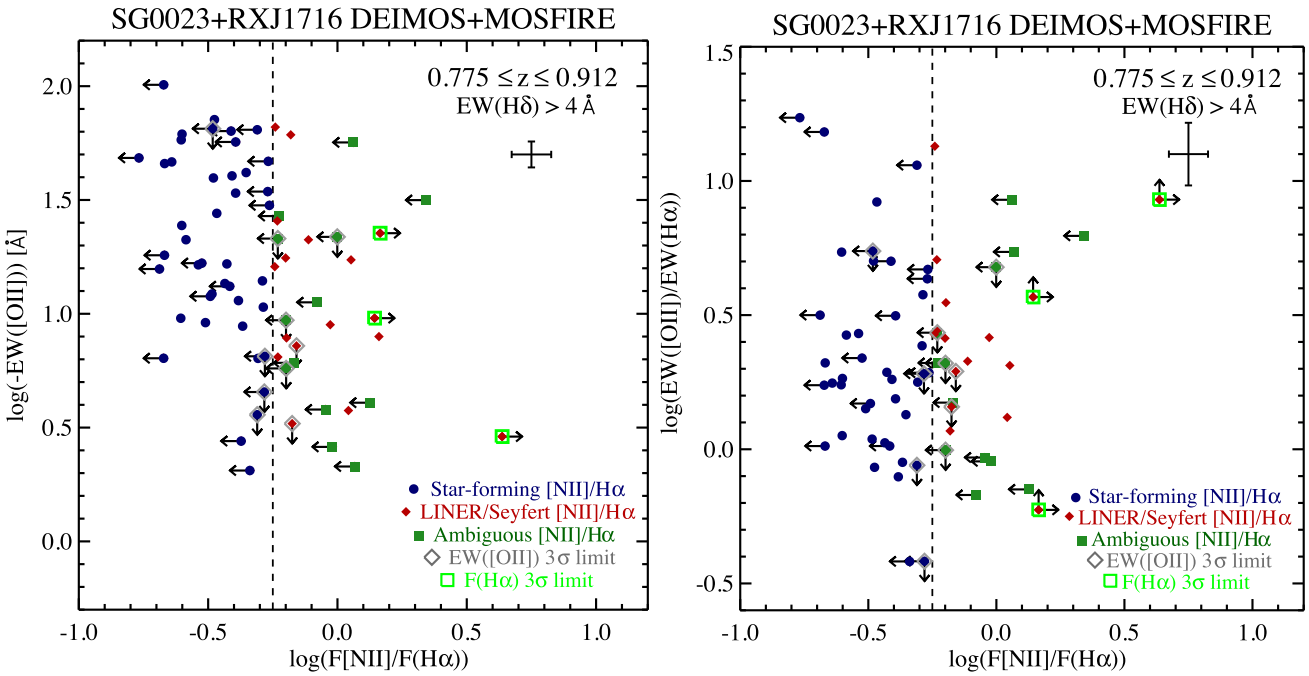

Figure 3. Left: Plot of (inverted) [O II] EW versus the emission line flux ratio of [N II]/H α for all MOSFIRE targets in the redshift range indicated with EW(H δ) > 4 Å and for which at least H α *or* [N II] were detected at a significant (>3σ) level. The dashed line demarcates galaxies dominated by LINER/Seyfert emission (log([N II]/Hα) ≥ -0.25) from those galaxies consistent with having some residual ongoing star formation activity (log([NII]/Hα) < -0.25). All galaxies with EW([O II] > -3 Å (see Section 2.3) are plotted by adopting their 3σ EW([O II]) limits and are shown with downward facing arrows and are circumscribed grey diamonds. These galaxies comprise the subset of traditional K+A galaxies targeted by MOSFIRE where H α or [N II] was significantly detected. Galaxies with a 3σ limit on [N II] are shown with leftward facing arrows, those with a 3σ limit on H α are shown with rightward facing arrows and are circumscribed by green boxes. Galaxies definitively classified as star-forming or LINER/Seyfert galaxies are shown as filled blue circles and red diamonds, respectively. Those galaxies whose limits on [N II]/H α were not sufficiently constraining are shown as darker green filled squares. The full sample of KAIROS galaxies is visible on this plot as those red diamonds not circumscribed by grey diamonds. Typical (median) errors for individual measurements are shown in the upper right portion of the panel. Right: Same as left, but with the EW ratio of [O II] and H α plotted on the ordinate. The meanings of symbols, arrows, and lines are the same. Only those galaxies for which we measured significant detection in both [N II] and [O II] and/or [N II] and H α are shown. The generally lower values of EW([O II])/EW(H α) exhibited by the KAIROS galaxies suggest that most have their emission powered by Seyfert or hybrid activity.

the H α emission (hereafter termed K+A-H α galaxies) we adopt as part of the true K+A population for the remainder of the paper.

Of the 69 priority II (starburst) galaxies at $0.775 \leq z \leq 0.912$ targeted with MOSFIRE, [N II]/H α classifications, through either significant detections of both lines or constraining limits, were made of 54. Of these, 39 had log([N II]/Hα) < -0.25 consistent with emission originating from star formation, the null hypothesis for these galaxies. However, 15 of these galaxies had [N II]/H α ratios (or lower limits) consistent with dominant LINER/Seyfert emission (log([N II]/Hα) ≥ -0.25). In such cases, the [O II] emission observed in the DEIMOS spectrum can also be attributed to a LINER/Seyfert process rather than star formation (Lemaux et al. 2010). Such galaxies are therefore spuriously classified by our DEIMOS spectra, as they have ceased star formation activity but show signs of a recently truncated ($\leq$1 Gyr) episode of star formation, the defining criteria of a K+A galaxy. For the remainder of the paper, such galaxies, which would be classified as K+A but for their relatively strong [O II] emission that is powered by a dominant LINER/Seyfert source (i.e. false-negative K+As) are referred to as K+A with ImposteR [O II]-derived star formation (KAIROS) galaxies. Applying these statistics to those priority II galaxies that either went untargeted with MOSFIRE or were unclassifiable to the depth of our observations results in ~50 KAIROS galaxies over the redshift range $0.775 \leq z \leq 0.912$, a value that *exceeds* the full traditional K+A sample in the same redshift range. Accounting for the impurity of the traditional K+A sample and including the estimated number of KAIROS galaxies in our full sample results in a true K+A fraction of 15.7 $\pm$ 1.7 per cent. Thus, not only does traditional selection of K+As at $z \sim 1$ result in a sample in which a moderate fraction of galaxies have ongoing star formation, but *such a selection also misses more than half of the true K+A population*. This fraction also does not change significantly if computed to the stellar mass completeness limit of our spectroscopic sample (see Table 4) nor if a different I^+ cut is imposed on the sample.

4.1.1 Environmental dependence of the post-starburst fraction

While we defer a complete analysis of the dependence of the two types of K+A fractions across different large-scale environments (i.e. field, group and cluster) and its dependence on various properties of LSSs to future work, we attempt here a cursory look. For this analysis we apply the statistics of the full sample and calculate fractions using all galaxies in the redshift range $0.775 \leq z \leq 0.912$. This choice was made to maximize the number of galaxies in each sub-sample we will define, though we note that results presented here largely hold if fractions are instead calculated only to the stellar mass completeness limit of our spectroscopic sample and/or by applying the statistics of each sub-sample separately. Group and cluster galaxies are defined broadly as those in the adopted SG0023 and RXJ1716 redshift ranges (see Section 2.2), with field galaxies defined as all galaxies that do not fall in the previous

Table 4. K+A fractions.

Sample	Traditional K+A fraction[a]	KAIROS/K+A-Hα fraction[a]	(KAIROS/K+A-Hα)/(SB+SF)
Full	7.7 ± 1.2 per cent (7.7 ± 1.3 per cent)	15.7 ± 1.7 per cent (15.3 ± 1.9 per cent)	–
LSSs Only	8.3 ± 1.5 per cent (8.5 ± 1.7 per cent)	15.6 ± 2.0 per cent (14.4 ± 2.2 per cent)	–
Field Only	4.4 ± 2.0 per cent	13.2 ± 3.4 per cent	20.6 ± 5.4 per cent
SG0023	7.2 ± 1.8 per cent	14.3 ± 2.7 per cent	21.5 ± 3.9 per cent
RXJ1716	10.1 ± 2.6 per cent	15.9 ± 3.3 per cent	29.3 ± 6.6 per cent

Note. [a] Where calculated, the numbers in parentheses give fractions for the stellar-mass-limited sample ($\log(\mathcal{M}_*/\mathcal{M}_\odot) \geq 10$).

two categories. Only those galaxies that were spectrally classifiable were used. Adopting the traditional K+A classification scheme results in K+A fractions of 4.4 ± 2.0 per cent, 7.2 ± 1.8 per cent and 10.1 ± 2.6 per cent amongst field, group and cluster galaxies, respectively. Such fractions and the trend of increasing traditional K+A fraction with increasing mass of the average central halo hosting the galaxy population is consistent with those observed in a variety of other $z \sim 1$ K+A studies (e.g. Tran et al. 2003, 2004; Poggianti et al. 2009; Muzzin et al. 2012; Wu et al. 2014). The observed trend is flattened considerably when comparing the combined KAIROS/K+A-Hα[9] fractions, which are 13.2 ± 3.4 per cent, 14.3 ± 2.7 per cent and 15.9 ± 3.3 per cent for the same three subsamples, respectively. At first glance, this lack of dependence seems to imply that more massive central haloes do not preferentially induce a K+A phase, contrary to results obtained for the vast majority of K+A studies at $z \sim 1$.

However, a slightly more nuanced approach can be taken. The number of K+A galaxies relative to the total number of combined starbursting and star-forming galaxies, hereafter K+A/(SB+SF), is a quantity more intimately linked with the efficacy of quenching processes. This fraction has been shown to be markedly higher amongst members of massive clusters and groups whose galaxy populations resemble those of more relaxed clusters (Poggianti et al. 2009) than the field or groups with a dominant star-forming population. Despite the similar true K+A fractions across the three sub-samples, a suggestive excess is observed in the true K+A/(SB+SF) fraction for cluster galaxies (29.3 ± 6.6 per cent) as compared to group or field galaxies (21.5 ± 3.9 per cent and 20.6 ± 5.4 per cent, respectively). As the vast majority of the SG0023 galaxy population is undergoing active star formation (∼70 per cent) and the groups show no large-scale X-ray emission indicative of an excessively harsh medium for the average group halo mass, the similarity of this fraction between the SG0023 members and in the field is perhaps not surprising. A similar trend was seen in a study of 11 groups at $z \sim 1$ (Mok et al. 2013) in which colour-selected, green 'transition' galaxies were found to comprise a consistent fraction of SB+SF galaxies relative to a coeval field sample at all stellar masses, though this fraction was seen to change dramatically as a function of stellar mass. The elevated fraction amongst the RXJ1716 members points to more efficient quenching within the bounds of the cluster, which, perhaps not coincidentally, is the only region in our sample definitively known to contain a hot medium. This trend is qualitatively similar to results found in the SC1604 supercluster, in which the only two constituent structures with detectable ICM emission (clusters A and B) exhibited both higher traditional K+A fractions and lower fractions of star-forming galaxies than all other clusters/groups within the supercluster as well as the coeval field (Lemaux et al. 2012; Wu et al. 2014). Though differing spatial and spectral selections and different breadth and depth of NIR spectroscopic coverage preclude a rigorous quantitative comparison between our sample and that presented in Wu et al. (2014), the completeness/purity-corrected, LINER/Seyfert-corrected true K+A/(SB+SF) fractions in clusters A and B range from ∼25 to 30 per cent as contrasted with ∼15 per cent for the galaxy populations of the SC1604 groups. These values are broadly consistent with those found amongst the galaxy population of SG0023 and RXJ1716. While this trend holds in our own data if we instead calculate these fractions for traditional K+As, these fractions decrease by a factor of 2–2.5× across all sub-samples. As the relative abundance of transitional populations is used to place constraints on quenching time-scales (e.g. Balogh et al. 2011, 2016; Mok et al. 2014; Muzzin et al. 2014), such a decrease can lead to drastically different conclusions on both the relative and absolute effectiveness of quenching mechanisms (Poggianti et al. 2009). In the following sections we investigate whether the shortcomings of traditional K+A selection are limited to lower purity and completeness or whether traditional K+As are composed of a distinct population from the sample selected here.

[9] This term will be used interchangeably with the term 'true K+A throughout the paper.

4.2 The evolutionary stages of K+A and KAIROS galaxies

We begin this investigation by comparing the average properties of traditional K+As and those K+As selected from the MOSFIRE+DEIMOS data. The latter sample is composed of both of known KAIROS galaxies and the pure population of traditional K+As, i.e. K+A-Hα galaxies (see Section 4.1). Galaxies selected using traditional K+A techniques appear, on average, both more massive in their stellar content ($\log(\langle\mathcal{M}_*\rangle/\mathcal{M}_\odot) = 10.65$ versus $\log(\langle\mathcal{M}_*\rangle/\mathcal{M}_\odot) = 10.35$) and redder ($M_{\rm NUV} - M_{r'} = 4.2$ versus $M_{\rm NUV} - M_{r'} = 4.0$) than the combined population of KAIROS/K+A-Hα galaxies. The two populations also appear at different positions in $M_{NUV} - M_{r'}$ versus $M_{r'} - M_J$ phase space, a phase space which is commonly employed to separate star-forming from quiescent populations. Traditional K+As, with average colours of 4.2 and 0.80, respectively, fall comfortably into the region of this phase space indicating quiescence (at $0.5 < z < 1$, see Lemaux et al. 2014), though in the region of this phase space is potentially also populated by recently ($\lesssim$1 Gyr) rapidly quenched galaxies (see e.g. Moutard et al. 2016). In moderate contrast, the average KAIROS/K+A-Hα galaxy, with colours of 4.0 and 0.85, respectively, appears in the liminal region of this phase space between star-forming and quiescent populations where younger transitional populations are likely to lie (Ilbert et al. 2010; Lemaux et al. 2014; Moutard et al. 2016). In Fig. 4 we plot $M_{\rm NUV} - M_{r'}$ versus $M_{r'} - M_J$ for all traditional K+A and KAIROS/K+A-Hα galaxies.

Such differences suggest that the true K+A population is predominantly younger than the K+A population selected using traditional means. While we, in principle, have estimates of the mean luminosity-weighted stellar age output by the SED fitting described

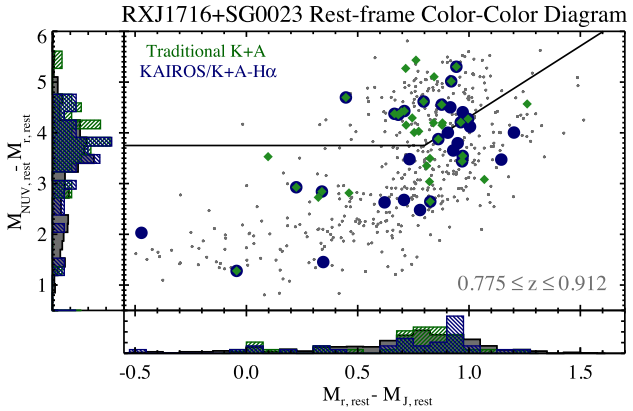

Figure 4. Rest-frame $M_{\rm NUV} - M_{r'}$ versus $M_{r'} - M_J$ distribution of all galaxies (small grey points) in SG0023 and RXJ1716 spectroscopically confirmed in the redshift range $0.775 \leq z \leq 0.912$. Overplotted are those galaxies that meet our criteria for traditional K+A (green diamonds) or KAIROS/K+A-Hα (blue circles). The black line shows the delination in this phase space between star-forming and quiescent galaxies adopted from Lemaux et al. (2014). Area normalized histograms are shown for all galaxies (grey filled), traditional K+As (green hatched), and KAIROS/K+A-Hα galaxies (blue hatched). The histograms in the left-hand panel are plotted as 'effective colour' defined as the distance away from the quiescent/star-forming dividing line. The two flavours of K+A galaxies have similar colours in this phase space, with KAIROS/K+A-Hα preferring slightly bluer $M_{\rm NUV} - M_{r'}$ and slightly redder $M_{r'} - M_J$ colours, possibly indicating a younger population on average (see Section 4.2).

in Section 3.1, age estimates from applying traditional SED-fitting techniques to broad-band photometry alone are highly uncertain (e.g. Lee et al. 2009; Pforr, Maraston & Tonini 2012; Thomas et al. 2017). Here, however, we have the luxury of high S/N DEIMOS spectra that contain several age-sensitive features [e.g. $D_n(4000)$, Hδ, G-band λ4305 Å]. These spectra in conjunction with the broad rest-frame wavelength coverage of our photometry allow us to place much stronger constraints on internal extinctions than is possible with the limited wavelength range of our DEIMOS spectroscopy. These constraints, in turn, largely allow for the breaking of the degeneracy between the stellar age of a galaxy and its dust content (as in Thomas et al. 2017, though at higher redshift), which subsequently allows for at least the potential of precision measurements on ages.[10]

The DEIMOS spectra of the two populations was combined (hereafter 'co-added') through an inverse variance-weighted average after shifting each individual spectrum to the rest frame, interpolating on to a standard grid with constant plate scale of $\Delta\lambda = 0.33/(1 + z_{\rm min})$ (where $z_{\rm min}$ is the minimum $z_{\rm spec}$ for each sample), and normalizing each spectrum to an average flux density of unity (e.g. unit weighted) following the methodology described in Lemaux et al. (2012). The resulting co-added spectra of the traditional K+A and the combined KAIROS and K+A-Hα population are shown in the left-hand panel of Fig. 5. The MOSFIRE spectra of the KAIROS/K+A-Hα population was also co-added in an identical manner (see Fig. 6). While this co-added MOSFIRE spectrum has continuum emission that is too faint to lend itself appreciably to the SED fitting process described here, the measure of the average [N II]/Hα of the resulting co-added spectra, $\log(\langle$[N II]/H$\alpha\rangle) = -0.09 \pm 0.02$, clearly establishes LINER/Seyfert activity as the dominant source of emission in these galaxies. The strength of the [S II] λ6716 Å line relative to Hα in the same spectrum was measured employing an identical method and custom bandpasses and found to be $\log(\langle$[S II]/H$\alpha\rangle) = -0.65 \pm 0.04$, a value constraining in its own right (see below).

It is important to pause at this point to consider several features of the co-added DEIMOS spectra presented in Fig. 5. The most striking difference is the strong [O II] feature of the average KAIROS/K+A-Hα galaxy (EW([O II]) $= -7.1 \pm 0.2$ Å), which is absent in the average traditional K+A spectrum. While some galaxies without strong [O II] emission are contained within the former sample (the K+A-Hα galaxies), these galaxies are subdominant to the KAIROS galaxies, which results in the observed strong [O II] emission. In addition, the high S/N of the co-added KAIROS/K+A-Hα spectrum allows us the luxury of significantly detecting the [Ne III] λ3868 Å line (EW([Ne III] $= -0.7 \pm 0.1$ Å). This measurement, when combined with that of [O II] and various colour measurements, strongly indicates the presence of activity other than star formation (Stasińska et al. 2006; Marocco, Hache & Lamareille 2011; Trouille, Barger & Tremonti 2011), though it is difficult to say definitively how much that activity dominates the emission profile based on these diagnostics alone. The most striking similarity between the two co-added spectra is the very strong Balmer series absorption observed both visually and quantitatively (EW(Hδ) $\sim 6.0 \pm 0.2$ Å in both cases) highlighting the large fractional population of A and B stars contained within the average galaxy in both populations (or, more precisely, the fraction of those stars not selectively affected by dust extinction; see e.g. Poggianti et al. 1999). Though less striking visually, the spectra exhibit significantly different strengths in the continuum break seen at 4000 Å $D_n(4000)$ (adopting the method of Balogh et al. 1999), 1.33 ± 0.01 versus 1.47 ± 0.01 for the average KAIROS/K+A-Hα galaxy and traditional K+A, respectively. Such a difference again strongly points to younger galaxies comprising the KAIROS/K+A-Hα population.

In parallel with this spectral coaddition, observed-frame broad-band photometry was co-added following the manner described in Appendix A. The co-added spectrum and photometry for each sample were then fit simultaneously to synthetic models (see Appendix A) to further investigate the evolutionary states of the two populations. In the right-hand panels of Fig. 5 we show a visualization of the results of this fitting process for a Bruzual (2007) model with the model parameters set to the values shown in each panel (for justification on these choices, see Appendix A). To make these visualizations, hereafter referred to as probability density maps (PDMs), the probability at each step in $t_{\rm SB}$ and $E_s(B-V)$ is calculated from the formula given in Appendix A, with $E_s(B-V)$ allowed to vary between 0 and 0.7 in steps of 0.05. It can be clearly seen in the PDMs that the dust-age degeneracy has been largely broken by this analysis, as there exists no anti-correlated behaviour between age and extinction in the observed PDMs. The vertical extent of the non-trivial values observed in the PDM in both cases is a result of the inability of our data to discriminate between various low levels of dust content. Below each panel shows the one-dimensional $t_{\rm SB}$ PDF generated by adding probabilities of all values of $E_s(B-V)$ for each age step. The median value of the PDF is denoted by a solid red vertical line. The effective $\pm 1\sigma$ values are taken from the 84th and 16th percentiles of the PDF, respectively, such that 68.3 per cent of the PDF is contained within their bounds. These effective $\pm$ 1σ values are shown as vertical dashed lines. The KAIROS/K+A-Hα population has a median $t_{\rm SB} = 0.75 \pm 0.19$ Gyr, younger than the corresponding value for the traditional K+A population

[10] Here and throughout the remainder of the paper 'age' is defined as the time since the onset of star formation and is denoted $t_{\rm SB}$.

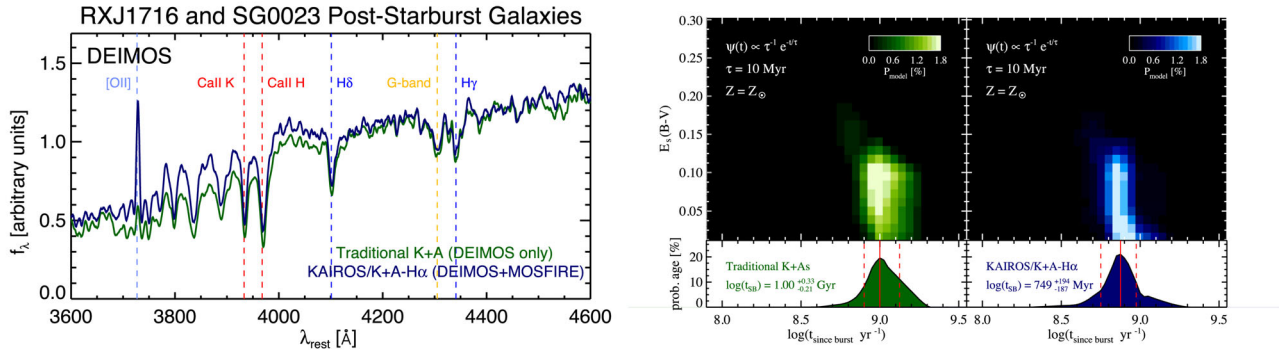

Figure 5. Left: Inverse-variance, unit-weighted co-added DEIMOS spectra of the traditional K+A (green) and KAIROS/K+A-H α (blue) galaxies. Important spectral features are marked by vertical dashed lines and labeled. The MOSFIRE spectra for the latter population was co-added in a similar manner (not shown) and the logarithm of the measured [N II]/H α ratio is given at the bottom of the figure. While the two DEIMOS co-added spectra appear to have similar strength Balmer features (Hγ, H δ, and higher order features blueward of Ca II K), strong [O II] emission attributable to a dominant LINER/Seyfert source (see Section 4.1) is present in the average KAIROS/K+A-H α galaxy spectrum. *Right:* Zoom in of the probability density maps (PDMs) for luminosity-weighted stellar ages and stellar extinctions of the average traditional K+A (upper left-hand panel) and KAIROS/K+A-H α (upper right-hand panel) galaxy estimated from fitting stellar synthesis models simultaneously to the stacked DEIMOS spectra and stacked photometry. In both panels, $\gg$99.9 per cent of the probability density of the full PDMs are contained within the displayed area. The form of the SFH, the e-folding time of the exponential decline, and the stellar-phase metallicity used for the fitting are given in the top left of each panel. A scale bar is shown in the top right of each panel and maps the colours to their associated probabilities. The bottom panels show the (extinction) marginalized one-dimensional PDFs of the luminosity-weighted stellar age for each sample. The median value of each PDF along with the associated effective 1σ uncertainties is reported in the left of each panel.

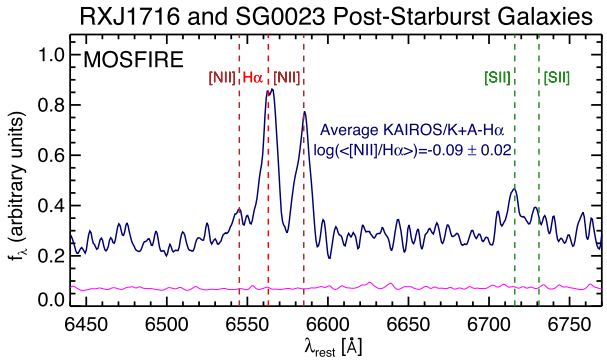

Figure 6. Inverse-variance, unit-weighted co-added MOSFIRE spectrum of the KAIROS/K+A-H α sample. The flux density spectrum is shown in blue and the error spectrum is shown in magenta. The location of H α and the [N II] λ6548 Å, λ6583 Å features is marked by dashed lines. Also marked are the locations of the S II λ6716 Å and 6731 Å features, both of which are significantly detected although appear to be relatively weak ($\log(\langle$[S II]/H$\alpha\rangle) = -0.65 \pm 0.04$ for the former feature). The average log([N II]/Hα) measurement derived from bandpass measurements on the spectrum is given. Such a value firmly excludes star formation as the dominant source of emission in these galaxies.

of $t_{SB} = 1.00^{+0.33}_{-0.21}$ Gyr. The distributions are not Gaussian, and the t_{SB} PDF of the average KAIROS/K+A-H α galaxy likely excludes the possibility (<10 per cent) that the average galaxy is older than the median t_{SB} of the traditional K+A population. These relative differences persist, at the same level of statistical significance, if we instead choose a different stellar synthesis prescription (BC03; Maraston 2005), SFH delayed τ, multi-burst, metallicity (0.2 $Z_\odot$, 0.4 $Z_\odot$), or extinction scheme (Prévot et al. 1984) for both sets of galaxies.

The combination of all analyses presented in this section strongly indicates that the true K+As are at an earlier evolutionary stage than those K+As selected using traditional methods. Adopting this possibility as truth, we then have a scenario in which a population of galaxies with a recently truncated massive star formation event with, on average, strong emission powered by a dominant LINER/Seyfert component evolves within ∼300 Myr to a population largely devoid of such emission. Such a scenario lends itself to the intriguing possibility that the source powering the LINER/Seyfert emission comes from residual AGN activity that was incited coevally (or nearly so) with the starburst. Other processes are known to give rise to LINER emission, galactic shocks (Dopita & Sutherland 1995; Veilleux et al. 1995), cooling flows (Heckman 1981; Heckman et al. 1989), photoionization by hot stars (Terlevich & Melnick 1985; Shields 1992), and post-asymptotic giant branch stars (Binette et al. 1994; Taniguchi, Shioya & Murayama 2000), and have been favoured over a central engine as powering LINER activity in recent results from spatially resolved spectroscopy (Singh et al. 2013; Belfiore et al. 2016), leading to a suggested change in terminology for such sources (Low Ionization Emission Regions). In this study, we do not have the luxury of spatially resolved spectroscopy. However, since such processes operate at different evolutionary phases and over different time-scales than AGN activity, the source of emission can, in principle, be uncovered through timing arguments or through other more direct observational means (see e.g. the discussion in Alatalo et al. 2016). Such timing arguments have been used on large samples of local post-starburst galaxies to argue that AGN activity is the dominant source of quenching for the most massive of such galaxies ($\log(\mathcal{M}_*/\mathcal{M}_\odot) > 10$; Kaviraj et al. 2007). While we make no serious effort to uncover the source of the emission in this paper, we note that most (80 per cent) of the galaxies definitively classified LINER/Seyfert have $\log(\mathrm{EW([O\,II])/EW(H}\alpha)) < 0.6$ (see Fig. 3), with a median value of $\log(\mathrm{EW([O\,II])/EW(H}\alpha)) = 0.4$. Such values are more typical of emission powered by Seyfert or hybrid activity rather than LINER-powered emission (Yan et al. 2006; Lemaux et al. 2010), which suggests that the narrow line emission in the KAIROS/K+A-H α sample originates from an AGN. Such a suggestion is in line with the relatively strong [Ne III] emission observed in the co-added KAIROS/K+A-H α DEIMOS spectrum (see e.g. Zeimann et al. 2015 and references therein). Additionally, the relatively weak [S II] λ6716 Å emission observed in the co-added KAIROS/K+A-H α MOSFIRE spectrum (see Fig. 6) appears to disfavour alternatives to AGN activity (see e.g. Kewley et al. 2006;

Alatalo et al. 2016). More detailed modelling will be required to explore this suggestion further and will be attempted in future studies. Here, we limit ourselves to searching for residual AGN activity through other more overt means, though any such activity is likely to be at a low level ∼700 Myr after the cessation of star formation (e.g. Hopkins et al. 2008).

We searched the ∼50 ks *Chandra* ACIS-I (Garmire et al. 2003) images obtained in both fields (Obs. IDs 7194 & 548 for SG0023 & RXJ1716, respectively; Vikhlinin et al. 2002; Rumbaugh et al. 2012) for individual detections of galaxies in both the traditional K+A and KAIROS samples. These images reach a 50 per cent completeness limit of $L_{X,0.5-7\mathrm{keV}} \gtrsim 10^{42.6}$ ergs s^{-1} at $z = 0.83$ over the area spanned by our sample as derived from Monte Carlo simulations (see Rumbaugh et al. 2017). No traditional K+A and only one galaxy from the KAIROS sample was individually matched to an X-ray source ($L_{X,0.5-7\mathrm{keV}} = 10^{42.7}$ ergs s^{-1}, log([N II]/Hα) = 0.68). We also preformed a stack of the X-ray data at the optical positions of the galaxies in two samples, separately, after removing the one X-ray detected KAIROS galaxy, sources at spatial locations coincident with the RXJ1716 ICM emission, and those at large (>7 arcmin) off-axis angles. No detection was found in either sample to a 3σ limit of $L_{X,0.5-7\mathrm{keV}} \sim 41.8$ at $\langle z \rangle = 0.83$.

It appears that any residual X-ray AGN activity in the KAIROS galaxies, if it exists, is generally too faint, both individually or on average, to observe with our data. In a study of traditionally selected K+As at $0.10 < z < 0.35$, no optically fainter K+As ($M_R > -22$) were observed with X-ray emission to a limit of $L_{X,0.5-7\mathrm{keV}} < 10^{41} - 10^{42}$ ergs s^{-1} (Brown et al. 2009). Galaxies at these luminosities comprise the bulk (∼75 per cent) of both our traditional K+A and KAIROS samples. While one third of optically brighter K+As ($M_R < -22$) are found to have nuclear X-ray activity in Brown et al. (2009), this activity was measured exclusively at levels below the 10 per cent completeness limit of our *Chandra* imaging. Such a paucity of nuclear activity was also observed by De Propris & Melnick (2014) in an extensive study of 10 local ($z \sim 0.03$) similarly optically faint traditionally selected K+As. Similarly weak X-ray emission was also observed in a sample of traditionally selected K+As drawn from the zCOSMOS-bright survey (Lilly et al. 2007) at redshifts more comparable to our sample. Using *Chandra* imaging considerably deeper than our own (Elvis et al. 2009), Vergani et al. (2010) found that only ∼10 per cent of their K+A sample exhibited detectable individual X-ray emission, all at $L_{X,0.5-10\ \mathrm{keV}} < 10^{43}$ ergs s^{-1}, and a stacking analysis of the remaining population revealed no significant detection to a limit comparable to that of our data (Vergani et al. 2010). Thus, the lack of coincident X-ray AGN activity in our current samples is likely not sufficiently constraining. It is also entirely possible that such activity is manifest in another mode, as strong X-ray and narrow-line activity from AGN are often times observed distinctly (Trouille et al. 2011; Yan et al. 2011). We defer further investigation of this scenario to the full population of ORELSE K+As for which we will be able to place extremely stringent limits on AGN activity, both for individual sources and for stacked data, from deeper X-ray, Very Large Array 1.4 GHz, NIR and MIR imaging, and more complex photoionization modelling.

4.3 Environments of post-starburst galaxies

We have shown in the previous sections that the inclusion of galaxies exhibiting K+A features with moderately strong [O II] emission powered by a LINER/Seyfert results in large changes in the number and type of galaxies selected as K+A. While we made a cursory attempt to investigate the effect of environment, defined in a broad sense, on the various post-starburst fractions in Section 4.1.1, in this section we investigate the distribution of the true K+A population across different environments and compare this distribution to traditional K+As and galaxies of other spectral types. As mentioned in Section 3.2, we chose here to use local overdensity as the sole metric for estimating environment. However, we note that within the limits of our data, none of the results presented in this section are sensitive to this choice. Identical results are obtained if we instead choose to perform the analysis based on group-/clusto-centric distance or in $R_{\mathrm{proj}}/R_{\mathrm{vir}} - |\Delta_{v,\mathrm{LOS}}|/\sigma_v$ phase space (see e.g. Carlberg et al. 1997; Balogh et al. 1999; Biviano et al. 2002; Haines et al. 2012; Noble et al. 2013). Since completeness now becomes an issue for our analysis, for this section, we limit the distributions for each galaxy sample to $\log(1 + \delta_{\mathrm{gal}}) \geq 0.5$. Above this value of overdensity we have obtained high-Q spectral measurements for which we can measure both EW([O II]) and EW(Hδ) reliably for ≥40 per cent of *all* objects in both fields (as estimated by our z_{phot} measurements), with an average completeness of 64 per cent, over the redshift range $0.775 \leq z \leq 0.912$, at $I^+ \leq 24.5$, and within the spatial extent covered by our DEIMOS masks coverage. With such a high level of spectroscopic completeness it is reasonable to assume that the distributions observed in our data are reflective of the true underlying distributions. In these environments MOSFIRE observations for which [N II]/Hα measurements were obtained (or meaningful limits placed) of traditional K+A and potential KAIROS galaxies is also high, 55 per cent and 45 per cent, respectively. Thus, such trends observed in the data are likely robust to sample variance.

In Fig. 7 we plot the cumulative $\log(1 + \delta_{\mathrm{gal}})$ distribution functions (CDFs) of quiescent, star-forming and starbursting galaxies along with the two flavours of K+A galaxies over roughly a decade and a half in local overdensity. A few broad initial observations can be made. While the distribution of quiescent galaxies appears largely similar, with quiescent galaxies preferring the densest environments in both fields and a Kolmogorov–Smirnov (KS) test finding no significant difference between the two populations, the environments of galaxies forming (relatively) modest amounts of stars (i.e. star-forming galaxies) are very different between the two fields. Star-forming galaxies strongly avoid the densest regions in the massive RXJ1716 cluster, while such galaxies are heavily clustered in the central regions of the SG0023 groups. In both cases starbursting galaxies generally avoid the densest regions, though with a stronger aversion to such regions seen in RXJ1716. These trends highlight the large range of evolutionary states of the LSSs in the two fields and underscore the necessity of accounting for both local (over)density and LSS properties (e.g. halo mass) when investigating environmentally driven galaxy evolution.

The environments of traditional K+A populations appear markedly different than the quiescent galaxies in SG0023. Such a trend is also observed for traditionally selected K+A member galaxies of the five groups in the SC1604 supercluster (Wu et al. 2014), using a different metric of environment (projected radius). We have independently confirmed that this trend holds in the SC1604 groups if $\log(1 + \delta_{\mathrm{gal}})$ (calculated as in Section 3.2) or projected positional-differential velocity phase space is instead used as an environmental metric and the same K+A selection techniques employed in this study are instead adopted. This concordance across 10 groups in two different fields strongly indicates that this is a general trend of K+A galaxies within groups. Conversely, traditional K+As and quiescent galaxies appear to show some overlap in their environments in RXJ1716, however, and a KS test cannot reject the possibility that the two distributions are drawn from the same

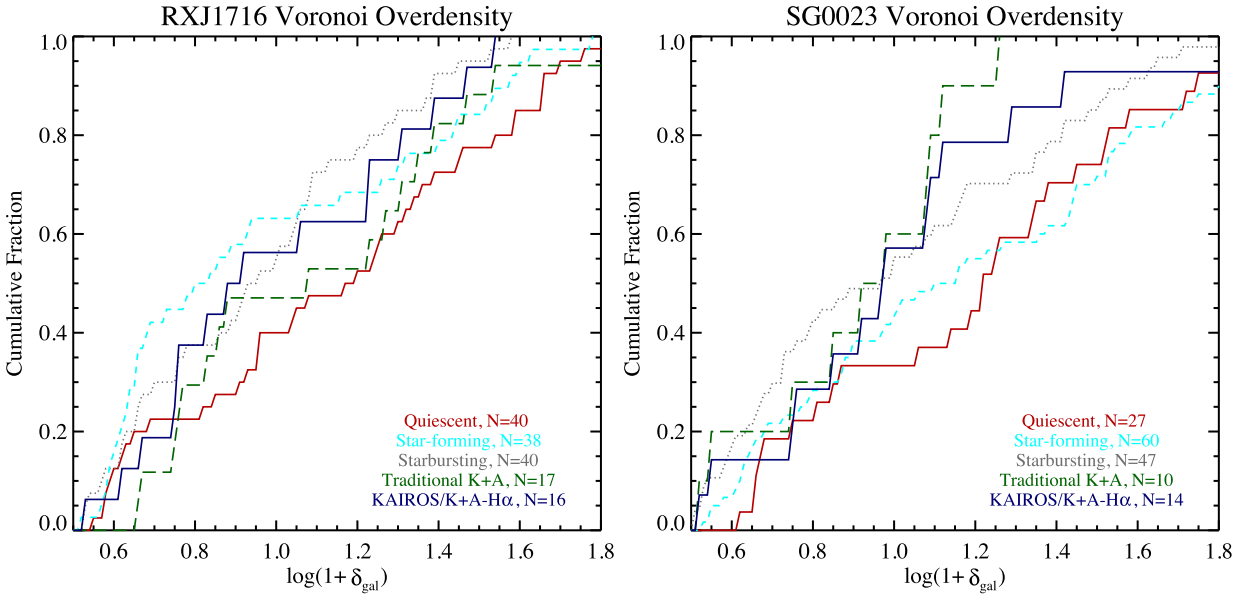

Figure 7. Overdensity cumulative distribution functions (CDFs) of various spectrally classed galaxies in the RXJ1716 (left) and SG0023 (right) fields in the redshift range $0.775 \leq z \leq 0.912$. The CDFs of quiescent, starbursting and star-forming galaxies are plotted with red solid, grey dotted and cyan dashed lines, respectively. The CDFs of the two flavours of K+As, traditional K+As and KAIROS/K+A-Hα, are shown by green long-dashed and blue solid lines, respectively. The majority of galaxies comprising each CDF are member galaxies of each LSS. Only galaxies with $I^{+} < 24.5$ and at $\log(1 + \delta_{\rm gal}) > 0.5$ are used to generate the CDFs as our DEIMOS observations are highly complete for such galaxies (see Section 4.3). MOSFIRE observations are also highly complete for the relevant galaxy populations (traditional K+A and starburst) when applying these cuts. The CDF of each galaxy type appears different in each field highlighting the effect of the differing LSS environment at common (local) overdensities. In each field, the CDFs of the traditional K+A and KAIROS/K+A-Hα galaxies are significantly different, with the latter largely tracing that of the starbursting population. In RXJ1716, the CDF of traditional K+As shows consistency with that of quiescent galaxies, a consistency not observed in SG0023, suggestive of a different evolutionary path.

underlying parent sample with any significance. Such overlap is also seen in the K+As housed in the three clusters of the SC1604 supercluster as well in preliminary results for other ORELSE clusters (RXJ1757, RXJ1821, SC1324, RCS0224) indicating that this is, again, a general trend of traditionally selected cluster K+As. The differences in the observed overlap between traditionally selected K+As and quiescent galaxies may have frustrated proper interpretation in previous studies that conflate group and cluster K+A populations or simply measure K+A properties and prevalence as a function of local density (or some other equally blunt environmental metric) without regard to the properties of the parent structure. No such ambiguity exists for the environments of the KAIROS/K+A-Hα galaxies, as a KS test firmly rejects ($\gg 3\sigma$) the hypothesis that their distribution is compatible with that of the quiescent population in both SG0023 and RXJ1716. This dissimilarity immediately precludes the possibility that, at least in the LSSs and their surrounding fields studied here, K+As are solely the products of rejuvenated quiescent galaxies (as in, e.g. Dressler et al. 2013). Instead, the KAIROS/K+A-Hα distributions appear to, more faithfully than those of the traditional K+As, track the environments of starbursts. In both RXJ1716 and SG0023 the environments of the traditional K+As are inconsistent with those of the starbursting population at $>3\sigma$, while those of the KAIROS/K+A-Hα populations are statistically indistinguishable in both cases.

4.3.1 Possible evolutionary scenarios for cluster and group post-starburst galaxies

The results in the previous section brought a dramatic shift in the interpretation of the possible progenitors of K+A galaxies. From a traditional K+A population moderately consistent with descending from quiescent galaxies, this study revealed the true K+A population within RXJ1716 and SG0023 almost certainly descended predominantly from bluer starbursting galaxies. As most of the quiescent galaxies are harbored, in both fields, within the cluster/group cores, this shifting interpretation also has dramatic consequences on the prevalence and efficacy of mechanisms acting on the K+A populations throughout their transformation. The more moderate-density environments (i.e. the outskirts of groups and clusters) inhabited by the true K+A population, where differential velocities remain relatively low, and their large environmental overlap with the starbursting population, a population known to exhibit a high fraction of disturbed morphologies (Kocevski et al. 2011; Kartaltepe et al. 2012; Pawlik et al. 2016), points to galaxy–galaxy interactions or merging activity as the primary formative events leading to the K+A phase. The latter activity in particular has been shown in simulations to effectively induce a K+A phase under certain conditions (Bekki et al. 2005; Johansson, Naab & Burkert 2009; Wild et al. 2009; Snyder et al. 2011).

While this result is seemingly at odds with the elevated true K+A/(SB+SF) fraction found for the galaxy population of the RXJ1716 cluster found in Section 4.1.1, the two results can be reconciled in the following manner. Interactions occurring near the outskirts (i.e. 1–2 $R_{\rm vir}$) of LSSs cause a starburst that decays over 10–100 Myr due either to gas exhaustion, stellar feedback (including supernovae), or feedback from an AGN. The massive reservoirs of H I or CO gas (the latter being a proxy for H_2) discovered surrounding ∼50 per cent of both field and group/cluster K+As in the local universe (Chang et al. 2001; Zwaan et al. 2013; French et al. 2015) points to the latter two mechanisms as both mechanisms can inject large amounts of kinetic energy into any remaining gas, disrupting star formation without, necessarily, completely removing the fuel supply. More recently, a study of SDSS K+A galaxies that were

selected in a similar manner to the KAIROS selection employed for this study found tentative evidence of widespread galactic winds in such galaxies driven by either AGN activity or stellar feedback processes (Alatalo et al. 2016). Such feedback is also consistent with that inferred from large surveys of dusty starbursting galaxies in both the local and distant universe in which the feedback is required to be relatively rapid (see Juneau et al. 2013; Lemaux et al. 2014, and references therein). These mechanisms also provide a natural explanation to explain the small values of $E_s(B-V)$ estimated in Section 4.2 as the same processes would also excise or diffuse the dust content near the inception of the K+A phase (as in, e.g. Yesuf et al. 2014). In field and group environments devoid of the presence of a well-formed hot medium, galaxies are largely allowed to retain this reservoir of hot gas, which is used to fuel rejuvenated star formation in ∼1–2 Gyr (e.g. Bahé & McCarthy 2015). Such a picture is consistent with the similar fraction of galaxies with active star formation (∼70 per cent) and those classified as starburst (∼28 per cent) in both environments as well as their similar fraction of true K+A/(SB+SF). In such a picture, the environmental distributions of KAIROS galaxies, galaxies that have residual signs of some form of this feedback (see Section 4.2), would appear more similar to starbursting galaxies, while traditional K+As, being further removed from the starbursting event, would start to diverge from the starbursting population. In neither case, however, should K+As follow the distributions of the quiescent populations, a restriction that holds for SG0023 K+As. Such fractions and distributions can be used to place constraints on the K+A duty cycle and will be attempted in future works.

The end stages of such a picture within a cluster environment would look considerably different. An initial starburst occurs near the cluster outskirts through galaxy interactions or merging events. Appealing to this method of inducement for RXJ1716 members is reasonable given that MIR-detected members of RXJ1716 (i.e. dusty starbursting galaxies) are seen to preferentially inhabit moderate local density environments within the overall LSS, roughly equivalent to our $\log(1+\delta_{\rm gal}) \lesssim 1$, and strongly avoid the region corresponding to the projected cluster core (Koyama et al. 2008). Such interactions lower the binding energy of the remaining gas through kinematic effects and stellar or AGN feedback, which allow it to be more easily stripped when entering the radius where strangulation and ram pressure stripping are effective ($\sim R_{\rm vir}$ and $\lesssim 0.5 R_{\rm vir}$, respectively, Moran et al. 2007, assuming for the latter a spherically symmetric ICM centred at the cluster optical centre, as is observed in RXJ1716). In a study of simulated cluster and group galaxies performed by Bahé & McCarthy (2015), it was found that the inclusion of stellar feedback doubles the effectiveness of ram pressure stripping on member galaxies of massive haloes even without including the (likely additive) effects of AGN feedback, which lends credence to this scenario. These interactions or merging events need not occur prior to the first pericentre passage of galaxies accreting into the cluster environment and, indeed, are perhaps more likely after this or several passages (see discussion in Struck 2006). Thus, such a scenario is still possible to reconcile with the 'delayed-then-rapid' quenching inferred by comparisons of observations of local cluster and group galaxies with numerical simulations (Wetzel et al. 2013) and the slightly less delayed-then-rapid quenching inferred from observations of other samples of $z \sim 1$ K+A galaxies (Muzzin et al. 2014) or other types of transitional populations observed at a variety of redshifts (Schawinski et al. 2014; Moutard et al. 2016).

In this scenario the K+A phase experienced by a cluster galaxy is largely not cyclic, but rather marks the end of a galaxy building up its stellar mass through *in situ* star formation. As a consequence, both the fraction of quiescent galaxies and the K+A/(SB+SF) fraction would elevate relative to those in less-dense environments, though the exact value of this increase depends on the length of the duty cycle of the K+A phase in the latter environments. Additionally, older (traditional) K+As would be observed to inhabit environments intermediate to those of starbursting and quiescent populations. All three trends are observed in the RXJ1716 galaxy population. Further supporting this scenario, ∼50 per cent of the traditional K+A and KAIROS/K+A-Hα galaxies that are members of the RXJ1716 cluster lie within $R_{\rm proj} < 0.5 R_{\rm vir}$ from the cluster centre. From the properties of its ICM emission, this radius is equivalent to the radius at which ram pressure stripping effectively acts on a Milky Way analog RXJ1716 member travelling at a radial velocity relative to the ICM equivalent to σ_v (see appendix B of Treu et al. 2003 for details on the calculation). Such a distribution is consistent with that observed in an exhaustive spectroscopic search for K+A galaxies in the massive $z \sim 0.55$ cluster MACS J0717.5+3745 (Ma et al. 2008) as well as published (Wu et al. 2014) and preliminary investigations of cluster K+A distributions in other ORELSE fields. In contrast, such a (projected) concentration for the two flavours of member K+As in SG0023 is not observed, as a majority of both types lie at larger ($R_{\rm proj} > 0.5 R_{\rm vir}\ h_{70}^{-1}$ Mpc) radii from the group centres. In this scenario, strangulation or ram pressure stripping acts in a maintenance role that forces galaxies in the K+A phase to persist in their quiescence after being acted upon by an (or several) initial, separate quenching mechanism(s).

Such cursory comparisons emphasize the importance of proper K+A selection in the task of determining their progenitors and the conditions necessary to invoke their presence. In this study we largely chose to proxy environment based on local overdensity. Since distributions of various populations, and, subsequently, inferences drawn from them, can be markedly different for different metrics of environment, and since our limited sample size precludes the possibility of further sub-dividing the samples presented here, we refrain here from attempting to compare this naive scenario to other more sophisticated scenarios for K+A evolution (e.g. Muzzin et al. 2014). The lines of investigation presented in this study, in concert with other metrics of environment and measures of morphological properties, will be followed further upon completion of the full sample.

5 CONCLUSIONS

In this study we used MOSFIRE to target a large number (∼100) of DEIMOS-selected traditional and potential K+A galaxies in and around two LSSs, SG0023 and RXJ1716, at $z \sim 0.83$ drawn from the ORELSE survey. Through measuring or placing constraining limits on the Hα emission and the [N II]/Hα emission ratio, these observations were used to quantify the fraction of galaxies included in traditional ($z \gtrsim 0.3$) K+A selection that are actively forming stars and the number of galaxies missed by traditional K+A selection due to spuriously ascribing [O II] emission to star-formation processes. A sample of true K+A galaxies was formed comprised of two populations, those traditional K+As without significant Hα emission or whose [N II]/Hα ratios did not indicate ongoing star formation (K+A-Hα galaxies) and those galaxies selected by our DEIMOS data to be starbursting for which we determined the dominant source powering the [O II] emission was either LINER or Seyfert activity (KAIROS galaxies). This sample of true K+A galaxies was used to compare to a variety of different aspects of the traditional K+A populations. Here we list the most important results of these comparisons.

(i) The sample of traditional K+A selected in and around SG0023 and RXJ1716 was found to have 25 per cent impurity, with contamination coming from dusty starbursting galaxies. Based on scaling the statistics of our MOSFIRE sample to the entire DEIMOS sample at $0.775 \leq z \leq 0.912$, we estimated that *traditional K+A selection misses more than half of the true K+A population*.

(ii) The traditional K+A fraction of our entire sample was found to be 7.7 ± 1.2 per cent as compared to the purity/completeness-corrected KAIROS/K+A-Hα fraction of 15.7 ± 1.7 per cent, with neither of these numbers changing significantly when calculating fractions to the stellar mass completeness limit of our DEIMOS sample.

(iii) While the traditional K+A fraction was found to vary considerably across different large-scale environments, 4.4 ± 2.0 per cent, 7.2 ± 1.8 per cent and 10.1 ± 2.6 per cent, for field galaxies, group and cluster members, respectively, the true K+A fraction was consistent with being constant across all large-scale environments. However, the number of KAIROS/K+A-Hα galaxies relative to the number of galaxies actively forming stars, K+A/(SB+SF), though constant amongst field galaxies and group members (20.6 ± 5.4 and 21.5 ± 3.9 per cent, respectively), was found to be considerably higher for cluster members (29.3 ± 6.6 per cent).

(iv) Traditional K+A galaxies were found on average to both contain more stellar mass and exhibit a moderately redder rest-frame $M_{\rm NUV} - M_{r'}$ colour than KAIROS/K+A-Hα galaxies. A combined fit of stacked DEIMOS spectra and optical/NIR photometry with a variety of stellar synthesis models revealed that the onset of the last major star-formation event in the average traditional K+A was appreciably earlier than that of the average KAIROS/K+A-Hα galaxy ($1.00^{+0.33}_{-0.21}$ Gyr versus 0.75 ± 0.19 Gyr, respectively), indicating that the former population possibly descended from the latter.

(v) Relatively strong [O II] and [Ne III] emission observed in the stacked DEIMOS spectrum of KAIROS/K+A-Hα galaxies (EW([O II]) $= -7.1 \pm 0.2$ Å, EW([Ne III] $= -0.7 \pm 0.1$ Å) as well as the relatively high log([N II]/Hα) ratio (-0.09 ± 0.02) observed in the stacked MOSFIRE spectrum strongly indicated the presence of either stellar or active galactic nuclei feedback. The relatively low values of EW([O II])/EW(Hα) observed for the bulk of the KAIROS sample along with the relatively high EW([Ne III])/EW([O II]) measured in their stacked DEIMOS spectra favoured the latter possibility. While X-ray emission was generally not detected in the KAIROS/K+A-Hα population either individually or in a stacked analysis, the size of our current sample, the depth of our X-ray imaging, and the cursory nature of this analysis did not allow us to rule out pervasive X-ray AGN activity in these galaxies.

(vi) When analysing the local overdensity distributions of (predominantly) member galaxies of the SG0023 supergroup and the massive RXJ1716 X-ray cluster, we found that the distributions of KAIROS/K+A-Hα were consistent with tracing the starbursting population and generally avoided the regions of highest (local) overdensity in both LSSs. In SG0023 the overdensity distribution of both the traditional K+As and the KAIROS/K+A-Hα galaxies was inconsistent with that of quiescent galaxies, while in RXJ1716 this distribution of K+As was indistinguishable from that of the quiescent population.

These lines of evidence were used to formulate a scenario in which true K+A galaxies evolve in a different manner in lower density large-scale environments (field and groups) than in cluster environments. In all cases, the K+A phase appears in galaxies inhabiting regions of moderate local overdensity relatively far removed from the cores of the groups or cluster. Such a distribution points to galaxy–galaxy interactions or mergers as *inducers* of the K+A phase rather than cluster- or massive group-specific processes such as ram pressure stripping. However, there does appear to be a signature of the latter processes at work on K+A galaxies in our data which is more subtle. Feedback from stellar or other processes is maintained for a considerable time after the cessation of star formation in the KAIROS/K+A-Hα galaxies (∼700 Myr). Such feedback, along with any initial stronger feedback associated with this cessation, serves to increase the thermal and kinetic energy in any remaining gas reservoir. In the field and in groups, those KAIROS/K+A-Hα galaxies whose feedback processes combined with any kinematic effects associated with the merger/interaction do not accelerate the gas to the escape velocity are largely allowed to retain their diffuse reservoirs of gas, as the effects of ram pressure stripping and strangulation are minimal or nonexistent in such environments. Such a scenario allows for the possibility of a cyclic K+A phase, a scenario consistent with the concordant fraction of starbursting, star-forming, and true K+A galaxies in these environments as well as the disparate overdensity distributions of traditional K+As and quiescent galaxies. In cluster environments, however, the effectiveness of mechanisms related to the stripping of hot or cold gas is enhanced by the decrease in the binding energy of that gas. As such, the K+A phase is rather a precursor to quiescence, with ram pressure stripping and/or strangulation acting in a *preventative* role that precludes the possibility reignited star formation. Such a scenario is consistent with both the observed overdensity distribution of traditional K+As and the elevated K+A/(SB+SF) fraction in RXJ1716. Future planned MOSFIRE observations of these fields and other LSSs in ORELSE along with cross-correlations of the wealth of multiwavelength data in the ORELSE survey will seek to calcify or reject this scenario. Deep, high-resolution imaging from the Atacama Large Millimeter/submillimeter Array (ALMA; Wootten & Thompson 2009) as well as observations of a large sample of K+A galaxies from adaptive-optics-fed integral field unit spectrometers, such as the one being developed for the Multi-Unit Spectroscopic Explorer (MUSE; Bacon et al. 2010) can also be extremely useful in challenging K+A formation scenarios (as in, e.g. Bekki et al. 2005) and how they evolve across different environments.

ACKNOWLEDGEMENTS

This material is based upon the work supported by the National Science Foundation under Grant No. 1411943. Part of the work presented herein is supported by NASA Grant Number NNX15AK92G. BCL thanks Nelson Cheung and Stephen Lampa for laying the foundation for this study and for looking through thousands of DEIMOS spectra for little glory and even less pay. BCL gratefully acknowledges Romain Thomas for discussions and guidance related to age estimates and Alison Mansheim and Lu Shen for discussions that improved the paper. We also thank the anonymous referee for helpful and careful guidance. This study is based, in part, on data collected at the Subaru Telescope and obtained from the SMOKA, which is operated by the Astronomy Data Center, National Astronomical Observatory of Japan. This work is based, in part, on observations made with the *SpitzerSpaceTelescope*, which is operated by the Jet Propulsion Laboratory, California Institute of Technology under a contract with NASA. UKIRT is supported by NASA and operated under an agreement among the University of Hawaii, the University of Arizona, and Lockheed Martin Advanced Technology Center; operations are enabled through the cooperation

of the East Asian Observatory. When the data reported here were acquired, UKIRT was operated by the Joint Astronomy Centre on behalf of the Science and Technology Facilities Council of the U.K. This study is also based, in part, on observations obtained with WIRCam, a joint project of CFHT, Taiwan, Korea, Canada, France, and the Canada-France-Hawaii Telescope, which is operated by the National Research Council (NRC) of Canada, the Institut National des Sciences de l'Univers of the Centre National de la Recherche Scientifique of France, and the University of Hawai'i. The scientific results reported in this article are based in part on observations made by the *Chandra* X-ray Observatory and data obtained from the *Chandra* Data Archive. The spectrographic data presented herein were obtained at the W.M. Keck Observatory, which is operated as a scientific partnership among the California Institute of Technology, the University of California, and the National Aeronautics and Space Administration. The Observatory was made possible by the generous financial support of the W.M. Keck Foundation. We wish to thank the indigenous Hawaiian community for allowing us to be guests on their sacred mountain, a privilege, without which, this work would not have been possible. We are most fortunate to be able to conduct observations from this site.

REFERENCES

Alatalo K. et al., 2016, ApJS, 224, 38
Alberts S. et al., 2016, ApJ, 825, 72
Ascaso B., Lemaux B. C., Lubin L. M., Gal R. R., Kocevski D. D., Rumbaugh N., Squires G., 2014, MNRAS, 442, 589
Bacon R. et al., 2010, in Ground-Based and Airborne Instrumentation for Astronomy III, p. 773508
Bahé Y. M., McCarthy I. G., 2015, MNRAS, 447, 969
Baldwin J. A., Phillips M. M., Terlevich R., 1981, PASP, 93, 5
Balogh M. L., Morris S. L., Yee H. K. C., Carlberg R. G., Ellingson E., 1999, ApJ, 527, 54
Balogh M. L., Miller C., Nichol R., Zabludoff A., Goto T., 2005, MNRAS, 360, 587
Balogh M. L. et al., 2011, MNRAS, 412, 2303
Balogh M. L. et al., 2016, MNRAS, 456, 4364
Bartholomew L. J., Rose J. A., Gaba A. E., Caldwell N., 2001, AJ, 122, 2913
Bekki K., Couch W. J., Shioya Y., Vazdekis A., 2005, MNRAS, 359, 949
Belfiore F. et al., 2016, MNRAS, 461, 3111
Belloni P., Bruzual A. G., Thimm G. J., Roser H.-J., 1995, A&A, 297, 61
Bertin E., Arnouts S., 1996, A&AS, 117, 393
Binette L., Magris C. G., Stasińska G., Bruzual A. G., 1994, A&A, 292, 13
Biviano A., Katgert P., Thomas T., Adami C., 2002, A&A, 387, 8
Brammer G. B., van Dokkum P. G., Coppi P., 2008, ApJ, 686, 1503
Brammer G. B. et al., 2011, ApJ, 739, 24
Brown M. J. I. et al., 2009, ApJ, 703, 150
Bruzual G., 2007, in Vallenari A., Tantalo R., Portinari L., Moretti A., eds, ASP Conf. Ser. Vol. 374, From Stars to Galaxies: Building the Pieces to Build Up the Universe, p. 303
Bruzual G., Charlot S., 2003, MNRAS, 344, 1000
Bundy K. et al., 2006, ApJ, 651, 120
Bundy K. et al., 2010, ApJ, 719, 1969
Butcher H., Oemler A., Jr, 1978, ApJ, 226, 559
Calzetti D., Armus L., Bohlin R. C., Kinney A. L., Koornneef J., Storchi-Bergmann T., 2000, ApJ, 533, 682
Carlberg R. G., Morris S. L., Yee H. K. C., Ellingson E., 1997, ApJ, 479, L19
Casali M. et al., 2007, A&A, 467, 777
Chabrier G., 2003, PASP, 115, 763
Chang T.-C., van Gorkom J. H., Zabludoff A. I., Zaritsky D., Mihos J. C., 2001, AJ, 121, 1965
Clowe D., Luppino G. A., Kaiser N., Henry J. P., Gioia I. M., 1998, ApJ, 497, L61
Cooke E. A. et al., 2016, ApJ, 816, 83
Cooper M. C. et al., 2007, MNRAS, 376, 1445
Couch W. J., Sharples R. M., 1987, MNRAS, 229, 423
Cucciati O. et al., 2017, A&A, 602, 15
Darvish B., Mobasher B., Sobral D., Scoville N., Aragon-Calvo M., 2015, ApJ, 805, 121
Darvish B., Mobasher B., Sobral D., Rettura A., Scoville N., Faisst A., Capak P., 2016, ApJ, 825, 113
Davidzon I. et al., 2013, A&A, 558, A23
Davis M. et al., 2003, in Guhathakurta P., ed., Proc. SPIE Vol. 4834, Discoveries and Research Prospects from 6- to 10-Metre-Class Telescopes II, p. 161
De Propris R., Melnick J., 2014, MNRAS, 439, 2837
De Propris R., Phillipps S., Bremer M. N., 2013, MNRAS, 434, 3469
Deng X.-F., Chen Y.-Q., Jiang P., 2011, MNRAS, 417, 453
Dey A., Lee K.-S., Reddy N., Cooper M., Inami H., Hong S., Gonzalez A. H., Jannuzi B. T., 2016, ApJ, 823, 11
Dopita M. A., Sutherland R. S., 1995, ApJ, 455, 468
Dressler A., 1980, ApJ, 236, 351
Dressler A., Gunn J. E., 1983, ApJ, 270, 7
Dressler A., Gunn J. E., 1992, ApJS, 78, 1
Dressler A., Smail I., Poggianti B. M., Butcher H., Couch W. J., Ellis R. S., Oemler A., Jr, 1999, ApJS, 122, 51
Dressler A., Jr, Oemler A., Poggianti B. M., Gladders M. D., Abramson L., Vulcani B., 2013, ApJ, 770, 62
Elvis M. et al., 2009, ApJS, 184, 158
Ettori S., Tozzi P., Borgani S., Rosati P., 2004, A&A, 417, 13
Faber S. M. et al., 2003, in Iye M., Moorwood A. F. M., eds, Society of Photo-Optical Instrumentation Engineers (SPIE) Conf. Ser. Vol. 4841, Instrument Design and Performance for Optical/Infrared Ground-Based Telescopes, p. 1657
Faber S. M. et al., 2007, ApJ, 665, 265
Falkenberg M. A., Kotulla R., Fritze U., 2009, MNRAS, 397, 1940
Fazio G. G. et al., 2004, ApJS, 154, 10
Fioc M., Rocca-Volmerange B., 1997, A&A, 326, 950
French K. D., Yang Y., Zabludoff A., Narayanan D., Shirley Y., Walter F., Smith J.-D., Tremonti C. A., 2015, ApJ, 801, 1
Fukugita M., Ichikawa T., Gunn J. E., Doi M., Shimasaku K., Schneider D. P., 1996, AJ, 111, 1748
Fumagalli M. et al., 2016, ApJ, 822, 1
Gal R. R., Lemaux B. C., Lubin L. M., Kocevski D., Squires G. K., 2008, ApJ, 684, 933
Garmire G. P., Bautz M. W., Ford P. G., Nousek J. A., Ricker G. R., Jr, 2003, in Truemper J. E., Tananbaum H. D., eds, Proc. SPIE Vol. 4851, X-Ray and Gamma-Ray Telescopes and Instruments for Astronomy, p. 28
Gómez P. L. et al., 2003, ApJ, 584, 210
Goto T. et al., 2003a, PASJ, 55, 739
Goto T., Yamauchi C., Fujita Y., Okamura S., Sekiguchi M., Smail I., Bernardi M., Gomez P. L., 2003b, MNRAS, 346, 601
Grazian A. et al., 2006, A&A, 449, 951
Gunn J. E., Gott J. R., III, 1972, ApJ, 176, 1
Haines C. P. et al., 2012, ApJ, 754, 97
Hansen S. M., Sheldon E. S., Wechsler R. H., Koester B. P., 2009, ApJ, 699, 1333
Heckman T. M., 1981, ApJ, 250, L59
Heckman T. M., Baum S. A., van Breugel W. J. M., McCarthy P., 1989, ApJ, 338, 48
Hopkins P. F., Hernquist L., Cox T. J., Kereš D., 2008, ApJS, 175, 356
Ilbert O. et al., 2006, A&A, 457, 841
Ilbert O. et al., 2010, ApJ, 709, 644
Ilbert O. et al., 2013, A&A, 556, A55
Johansson P. H., Naab T., Burkert A., 2009, ApJ, 690, 802
Jones T., Martin C., Cooper M. C., 2015, ApJ, 813, 126
Juneau S. et al., 2013, ApJ, 764, 176
Kannappan S. J., Guie J. M., Baker A. J., 2009, AJ, 138, 579

Kartaltepe J. S. et al., 2012, ApJ, 757, 23
Kauffmann G. et al., 2003, MNRAS, 346, 1055
Kaviraj S., Kirkby L. A., Silk J., Sarzi M., 2007, MNRAS, 382, 960
Kennicutt R. C., Jr, 1998, ARA&A, 36, 189
Kewley L. J., Groves B., Kauffmann G., Heckman T., 2006, MNRAS, 372, 961
Kewley L. J., Dopita M. A., Leitherer C., Davé R., Yuan T., Allen M., Groves B., Sutherland R., 2013a, ApJ, 774, 100
Kewley L. J., Maier C., Yabe K., Ohta K., Akiyama M., Dopita M. A., Yuan T., 2013b, ApJ, 774, L10
Kocevski D. D. et al., 2011, ApJ, 736, 38
Koyama Y. et al., 2008, MNRAS, 391, 1758
Kriek M., van Dokkum P. G., Labbé I., Franx M., Illingworth G. D., Marchesini D., Quadri R. F., 2009, ApJ, 700, 221
Laigle C. et al., 2016, ApJS, 224, 24
Lamareille F. et al., 2009, A&A, 495, 53
Landolt A. U., 1992, AJ, 104, 340
Le Borgne D. et al., 2006, ApJ, 642, 48
Le Fèvre O. et al., 2013, A&A, 559, A14
Lee S.-K., Idzi R., Ferguson H. C., Somerville R. S., Wiklind T., Giavalisco M., 2009, ApJS, 184, 100
Lemaux B. C., Lubin L. M., Shapley A., Kocevski D., Gal R. R., Squires G. K., 2010, ApJ, 716, 970
Lemaux B. C. et al., 2012, ApJ, 745, 106
Lemaux B. C. et al., 2014, A&A, 572, A90
Lemaux B. C. et al., 2017a, A&A, preprint (arXiv:1703.10170)
Lemaux B. C. et al., 2017b, MNRAS, submitted
Lilly S. J. et al., 2007, ApJS, 172, 70
Lin L. et al., 2016, ApJ, 817, 97
Lubin L. M., Gal R. R., Lemaux B. C., Kocevski D. D., Squires G. K., 2009, AJ, 137, 4867
Makovoz D., Marleau F. R., 2005, PASP, 117, 1113
Ma C.-J., Ebeling H., Donovan D., Barrett E., 2008, ApJ, 684, 160
Maltby D. T. et al., 2016, MNRAS, 459, L114
Maraston C., 2005, MNRAS, 362, 799
Marocco J., Hache E., Lamareille F., 2011, A&A, 531, A71
Martini P. et al., 2013, ApJ, 768, 1
Masters K. L. et al., 2010, MNRAS, 405, 783
McLean I. S. et al., 2012, in Ground-Based and Airborne Instrumentation for Astronomy IV, p. 84460J
Melnick J., De Propris R., 2013, MNRAS, 431, 2034
Merlin E. et al., 2015, A&A, 582, A15
Miyazaki S. et al., 2002, PASJ, 54, 833
Mok A. et al., 2013, MNRAS, 431, 1090
Mok A. et al., 2014, MNRAS, 438, 3070
Moran S. M., Ellis R. S., Treu T., Smith G. P., Rich R. M., Smail I., 2007, ApJ, 671, 1503
Moutard T. et al., 2016, A&A, 590, A103
Muzzin A. et al., 2012, ApJ, 746, 188
Muzzin A. et al., 2014, ApJ, 796, 65
Newberry M. V., Boroson T. A., Kirshner R. P., 1990, ApJ, 350, 585
Newman J. A. et al., 2013, ApJS, 208, 5
Noble A. G., Webb T. M. A., Muzzin A., Wilson G., Yee H. K. C., van der Burg R. F. J., 2013, ApJ, 768, 118
Noble A. G., Webb T. M. A., Yee H. K. C., Muzzin A., Wilson G., van der Burg R. F. J., Balogh M. L., Shupe D. L., 2016, ApJ, 816, 48
Oemler A., Jr, 1974, ApJ, 194, 1
Oemler A., Jr, Dressler A., Kelson D., Rigby J., Poggianti B. M., Fritz J., Morrison G., Smail I., 2009, ApJ, 693, 152
Oke J. B., Gunn J. E., 1983, ApJ, 266, 713
Ouchi M. et al., 2004, ApJ, 611, 660
Papovich C. et al., 2010, ApJ, 716, 1503
Pawlik M. M., Wild V., Walcher C. J., Johansson P. H., Villforth C., Rowlands K., Mendez-Abreu J., Hewlett T., 2016, MNRAS, 456, 3032
Peng Y.-j. et al., 2010, ApJ, 721, 193
Pérez-Montero E. et al., 2009, A&A, 495, 73
Pérez-Montero E. et al., 2013, A&A, 549, A25
Pforr J., Maraston C., Tonini C., 2012, MNRAS, 422, 3285
Pickles A. J., 1998, PASP, 110, 863
Poggianti B. M., Smail I., Dressler A., Couch W. J., Barger A. J., Butcher H., Ellis R. S., Oemler A., Jr, 1999, ApJ, 518, 576
Poggianti B. M. et al., 2009, ApJ, 693, 112
Pozzetti L. et al., 2010, A&A, 523, A13
Prévot M. L., Lequeux J., Prevot L., Maurice E., Rocca-Volmerange B., 1984, A&A, 132, 389
Puget P. et al., 2004, in Moorwood A. F. M., Iye M., eds, Proc. SPIE Vol. 5492, Ground-Based Instrumentation for Astronomy, p. 978
Rumbaugh N. et al., 2017 MNRAS, 466, 496
Rumbaugh N., Kocevski D. D., Gal R. R., Lemaux B. C., Lubin L. M., Fassnacht C. D., McGrath E. J., Squires G. K., 2012, ApJ, 746, 155
Rumbaugh N., Kocevski D. D., Gal R. R., Lemaux B. C., Lubin L. M., Fassnacht C. D., Squires G. K., 2013, ApJ, 763, 124
Ryan R. E., Jr, et al., 2014, ApJ, 786, L4
Sanders R. L. et al., 2015, ApJ, 799, 138
Santos J. S. et al., 2014, MNRAS, 438, 2565
Santos J. S. et al., 2015, MNRAS, 447, L65
Schawinski K. et al., 2014, MNRAS, 440, 889
Shapley A. E. et al., 2015, ApJ, 801, 88
Shields J. C., 1992, ApJ, 399, L27
Simcoe R. A., Metzger M. R., Small T. A., Araya G., 2000, in American Astronomical Society Meeting Abstracts #196. p. 758
Singh R. et al., 2013, A&A, 558, A43
Skrutskie M. F. et al., 2006, AJ, 131, 1163
Snyder G. F., Cox T. J., Hayward C. C., Hernquist L., Jonsson P., 2011, ApJ, 741, 77
Stasińska G., Cid Fernandes R., Mateus A., Sodré L., Asari N. V., 2006, MNRAS, 371, 972
Strazzullo V. et al., 2010, A&A, 524, A17
Struck C., 2006, Galaxy Collisions – Dawn of a New Era, p. 115
Swinbank A. M., Balogh M. L., Bower R. G., Zabludoff A. I., Lucey J. R., McGee S. L., Miller C. J., Nichol R. C., 2012, MNRAS, 420, 672
Taniguchi Y., Shioya Y., Murayama T., 2000, AJ, 120, 1265
Taranu D. S., Hudson M. J., Balogh M. L., Smith R. J., Power C., Oman K. A., Krane B., 2014, MNRAS, 440, 1934
Terlevich R., Melnick J., 1985, MNRAS, 213, 841
Thomas R. et al., 2017, A&A, 602, 35
Tody D., 1993, in Hanisch R. J., Brissenden R. J. V., Barnes J., eds, ASP Conf. Ser. Vol. 52, Astronomical Data Analysis Software and Systems II, p. 173
Tomczak A. R. et al., 2017, MNRAS, submitted
Tran K.-V. H., Franx M., Illingworth G., Kelson D. D., van Dokkum P., 2003, ApJ, 599, 865
Tran K.-V. H., Franx M., Illingworth G. D., van Dokkum P., Kelson D. D., Magee D., 2004, ApJ, 609, 683
Tran K.-V. H., Franx M., Illingworth G. D., van Dokkum P., Kelson D. D., Blakeslee J. P., Postman M., 2007, ApJ, 661, 750
Tran K.-V. H. et al., 2010, ApJ, 719, L126
Treu T., Ellis R. S., Kneib J.-P., Dressler A., Smail I., Czoske O., Oemler A., Natarajan P., 2003, ApJ, 591, 53
Treu T. et al., 2005, ApJ, 633, 174
Trouille L., Barger A. J., Tremonti C., 2011, ApJ, 742, 46
van der Burg R. F. J. et al., 2013, A&A, 557, A15
Veilleux S., Kim D.-C., Sanders D. B., Mazzarella J. M., Soifer B. T., 1995, ApJS, 98, 171
Vergani D. et al., 2010, A&A, 509, A42
Vikhlinin A., van Speybroeck L., Markevitch M., Forman W. R., Grego L., 2002, ApJ, 578, L107
Vulcani B. et al., 2013, A&A, 550, A58
Wang T. et al., 2016, ApJ, 828, 56
Webb T. M. A. et al., 2013, AJ, 146, 84
Werner M. W. et al., 2004, ApJS, 154, 1
Wetzel A. R., Tinker J. L., Conroy C., van den Bosch F. C., 2013, MNRAS, 432, 336
Wild V., Walcher C. J., Johansson P. H., Tresse L., Charlot S., Pollo A., Le Fèvre O., de Ravel L., 2009, MNRAS, 395, 144
Wild V. et al., 2014, MNRAS, 440, 1880

Wootten A., Thompson A. R., 2009, IEEE Proc., 97, 1463
Wu P.-F., Gal R. R., Lemaux B. C., Kocevski D. D., Lubin L. M., Rumbaugh N., Squires G. K., 2014, ApJ, 792, 16
Yan R., Newman J. A., Faber S. M., Konidaris N., Koo D., Davis M., 2006, ApJ, 648, 281
Yan R. et al., 2009, MNRAS, 398, 735
Yan R. et al., 2011, ApJ, 728, 38
Yesuf H. M., Faber S. M., Trump J. R., Koo D. C., Fang J. J., Liu F. S., Wild V., Hayward C. C., 2014, ApJ, 792, 84
York D. G. et al., 2000, AJ, 120, 1579
Yuan T.-T., Kewley L. J., Richard J., 2013, ApJ, 763, 9
Zabludoff A. I., Zaritsky D., Lin H., Tucker D., Hashimoto Y., Shectman S. A., Oemler A., Kirshner R. P., 1996, ApJ, 466, 104
Zahid H. J., Kewley L. J., Bresolin F., 2011, ApJ, 730, 137
Zeimann G. R. et al., 2013, ApJ, 779, 137
Zeimann G. R. et al., 2015, ApJ, 798, 29
Ziparo F. et al., 2014, MNRAS, 437, 458
Zwaan M. A., Kuntschner H., Pracy M. B., Couch W. J., 2013, MNRAS, 432, 492

APPENDIX A: SIMULTANOUS SPECTRAL ENERGY DISTRIBUTION FITTING OF SPECTRA AND PHOTOMETRY

Here we describe the process of co-adding the broad-band magnitudes and the simultaneous fitting of the co-added spectra and photometry used to generate the results presented in Section 4.2. In order to co-add the broad-band photometry, a scaling factor was applied to the photometry of each galaxy such that the average flux density of the combined I^+ and Z^+ bands was unity. This scaling factor was applied to all bands prior to co-addition. This choice was motivated by our desire to match the normalization of the spectral co-adding process described in Section 4.2, as the central observed-frame wavelength coverage of our DEIMOS spectroscopy roughly lies at the border between the I^+ and Z^+ bands. The (normalized) flux density for each band was then calculated by an inverse variance-weighted mean after removing, for each galaxy, bands in which that galaxy went undetected ($<3\sigma$). An small (3 per cent) additional systematic uncertainty was included in the formal random uncertainty of the co-added flux density in each band to account for uncertainty in the photometric zero-points (see e.g. Ilbert et al. 2006; Brammer et al. 2008).

The resultant co-added spectra and photometry for the traditional K+A and KAIROS/K+A-Hα samples were then compared to a suite of synthetic spectral models (BC03; Maraston 2005; Bruzual 2007) after linearly interpolating over the [O II] feature. For each prescription a variety of SFHs ($\psi(t)$), stellar-phase metallicities and stellar continuum extinctions were employed, with each model generated for ages in the range $\log(t_{\rm SB}) = 7$–9.6 in 24 steps roughly equally spaced in $log(t_{\rm SB})$. For the spectral comparison, co-added spectra were degraded through spline interpolation to match the plate scale of the models. For the photometric comparison, synthetic model magnitudes were created by convolving models with the appropriate filter curves shifted to the average redshift of the sample. Only those wavelength ranges for which 100 per cent of the galaxies contributed to the co-added spectra and photometry were considered in the models. The probability of a certain parameter/model combination was calculated at each age step as $e^{-(0.5\chi^2_{\nu,\rm spec}+0.5\chi^2_{\nu,\rm phot})/2}$, where $\chi^2_{\nu,\rm spec}$ and $\chi^2_{\nu,\rm phot}$ are the reduced χ^2 calculated from the comparison of co-added spectra and photometry, respectively, to the model at this step (see Thomas et al. 2017 for details).

While this machinery can be, in principle, used to generate combined probabilities for all combinations of parameters and models, such a large range of allowable values quickly becomes computationally untenable and massively underconstrained astrophysically. Instead, we chose for this analysis to place two strong constraints on the models used. The first is that the SFH of the model(s) used for the fit be exponentially declining with a short e-folding time. Such an SFH does not preclude the possibility of star formation in a continuous or bursty mode prior to this decline, but this prior requires that the cessation of star formation, once begun, proceed rapidly (here we choose $\tau = 10$ Myr, where $\psi(t) \propto \tau^{-1}\exp\,-t/\tau$). Such an SFH essentially defines a K+A galaxy (e.g. Poggianti et al. 1999) and thus represents a reasonable assumption.

The second constraint is placed on the stellar-phase metallicity, a parameter that, if left unconstrained, can wreak havoc on age measurements (e.g. Fumagalli et al. 2016). In the absence of the ability to measure the gas- or stellar-phase metallicity directly, the mean stellar masses of the traditional K+A and KAIROS/K+A-Hα samples can be used to place strong constraints on the gas-phase metallicity from the mass-metallicity relation. Such constraints are, in turn, linked to the average stellar-phase metallicity by virtue of the rapid formation of the luminosity-dominant stellar population recently formed in our samples. Results from analysing the largest samples of star-forming galaxies at $z \sim 0.8$ currently available place the average gas-phase metallicity of galaxies at stellar masses equal to the average of both of our samples at approximately solar (Lamareille et al. 2009; Pérez-Montero et al. 2009; Zahid, Kewley & Bresolin 2011; Pérez-Montero et al. 2013; Yuan, Kewley & Richard 2013). Thus, we explicitly impose that the models used be generated with what is referred to as $Z = Z_{\odot}$ in the stellar synthesis models. In addition, we adopt the prescription of Bruzual (2007) for this fitting as these models, generally, provided a slightly better fit to our data than either the BC03 or Maraston models for a given combination of parameters. It is crucial to note that the relative comparisons made in this paper are *completely insensitive* to variations in $\psi(t)$, stellar-phase metallicity, and prescription as long as the same choice is made for both samples, and only result in absolute offsets in $t_{\rm SB}$. These relative comparisons also hold if we instead choose an SFH parametrized by a galaxy undergoing a rejuvination event of variable strength (5–20 per cent by stellar mass) at a variety of different times (2–3 Gyr) after the onset of its initial star formation event or a delayed τ model.

This paper has been typeset from a TEX/LATEX file prepared by the author.